Materials & Design 266 (2026) 116230

Contents lists available at ScienceDirect

Materials & Design

journal homepage: www.elsevier.com/locate/matdes

Synchrotron and AI-enabled large-scale 3D morphometric analysis of osteocyte lacunae reveals disease-associated microstructural remodeling in human trabecular bone

Seyedeh Fahimeh Hosseini [a], Isabella Poles [b], Eleonora D'Arnese [c], Barbara Canciani [d], Laura Maria Vergani [a,*], Federica Buccino [a]

[a] Department of Mechanical Engineering (DMEC), Politecnico di Milano, Via La Masa 1, 20156 Milan, Italy
[b] Department of Electronics Information and Bioengineering, Politecnico di Milano, 20133 Milan, Italy
[c] School of Informatics, University of Edinburgh, Edinburgh, Scotland, United Kingdom
[d] IRCCS Galeazzi-Sant'Ambrogio, Via Cristina Belgioioso 173, 20157 Milan, Italy

ARTICLE INFO

Keywords:
Osteocyte lacunae
Lacunar morphology
Synchrotron
Osteoporosis
Bone microstructure

ABSTRACT

Bone fragility in Osteoporosis and following COVID-19 infection has been increasingly reported at the tissue level; however, direct human evidence linking these conditions to alterations in osteocyte lacunar micro-architecture remains limited. Osteocyte lacunae form the mechanosensory network of bone, where geometry modulates local strain amplification and fluid flow. Quantitative characterization of disease-associated lacunar remodeling in human trabecular bone has been constrained by imaging resolution and sample size. Trabecular bone from 48 human female femoral heads (Healthy, Osteoporosis, and post–COVID-19; $n = 16$ per group) was analyzed using synchrotron phase-contrast micro-CT combined with AI-based recognition of relevant features. Approximately 8.96 million lacunae were quantified, enabling large-scale extraction of three-dimensional morphometric descriptors. Osteoporosis was associated with significantly larger lacunae than post–COVID-19 bone ($p < 0.05$), reflected by increased volume, surface area, and semi-minor axis length, while healthy bone showed intermediate values. Lacunar sphericity and BV/TV were significantly reduced in Osteoporosis ($p = 0.019$), whereas lacunar density did not differ among groups, indicating geometric remodeling rather than changes in lacunar abundance. These findings establish a quantitative benchmark for disease-associated lacunar remodeling in human trabecular bone and demonstrate that osteocyte lacunar geometry captures microstructural signatures not reflected by densitometric measures alone.

1. Introduction

Osteocytes are the most abundant cells in bone and form a highly interconnected lacunocanalicular network that orchestrates mechanosensation and remodeling [1–3]. The three-dimensional geometry of the osteocyte lacuna, its volume, surface morphology, shape anisotropy, and spatial orientation, governs local strain amplification and interstitial fluid flow, thereby modulating the mechanical signals transmitted to the osteocyte cell body [4–6]. Because osteocyte-driven mechanotransduction regulates both bone formation and resorption, lacunar morphology is not merely a structural descriptor but a functional determinant of tissue adaptation. Subtle alterations at the lacunar scale may therefore precede macroscopic deterioration and reflect early shifts in bone quality, particularly in aging and pathological conditions, such as osteoporosis, where remodeling dynamics are altered [7,8].

Clinically, bone mineral density (BMD) derived from dual-energy X-ray absorptiometry (DEXA) remains the primary diagnostic metric for osteoporosis. However, areal BMD captures only mineral quantity and does not reflect microarchitectural organization, material heterogeneity, or the cellular microenvironment that collectively determine fracture resistance [9,10]. Notably, a substantial proportion of fragility fractures occur in individuals whose BMD values do not fall within the osteoporotic range, underscoring the need for quantitative biomarkers capable of probing bone quality beyond mineral density alone [5,11]. In this context, osteocyte lacunar morphometry represents a promising microstructural biomarker, as it directly characterizes the structural

---

* Corresponding author.
E-mail address: laura.vergani@polimi.it (L.M. Vergani).

https://doi.org/10.1016/j.matdes.2026.116230
Received 16 March 2026; Received in revised form 1 May 2026; Accepted 13 May 2026

environment of the mechanosensory network that regulates remodeling.

Recent advances in synchrotron phase-contrast micro-computed tomography (micro-CT) enable three-dimensional visualization of osteocyte lacunae at sub-micron resolution, allowing precise quantification of volume, surface area, shape descriptors, and principal-axis orientation [8,12–17]. Prior studies have demonstrated that lacunar morphology varies with age, anatomical location, and mechanical environment [8,12,15,18], and pathology-associated differences have been reported in specific contexts, including hypermineralized lacunae in osteoporotic bone suggestive of impaired remodeling [19–21]. However, findings across studies remain heterogeneous, with some investigations reporting minimal or context-dependent differences between osteoporotic and control cohorts [19–21]. Such variability likely reflects differences in anatomical site, imaging protocols, segmentation strategies, and sample size, highlighting the need for standardized, large-scale analyses in human bone.

Despite increasing interest in lacunar morphometry, its quantitative analysis in human trabecular bone remains limited. Much of the foundational work has focused on cortical compartments, whereas trabecular regions at clinically relevant fracture sites, such as the femoral head, remain less exhaustively characterised [17]. Trabecular bone is particularly relevant in this context, as it exhibits higher metabolic activity and remodeling rates than cortical bone, making it more sensitive to pathological changes. Moreover, clinically relevant fragility fractures frequently originate in trabecular-rich regions, such as the femoral head and vertebrae, highlighting its importance for understanding disease-related alterations in bone quality. Additionally, most available studies rely on relatively small sample sizes, limiting statistical power and the ability to distinguish lacuna-level variability from patient-level heterogeneity. Large-scale, hierarchical analytical frameworks that explicitly account for the nested structure of lacunae within individuals are therefore required to define robust disease-associated lacunar signatures.

In parallel, emerging experimental and clinical evidence indicates that systemic inflammatory conditions, including post-COVID-19, may disrupt bone metabolism by increasing osteoclast activity, reducing trabecular bone mass, and altering osteogenic markers [22–25]. Indirect consequences of the pandemic, including interruption of osteoporosis therapies, have further contributed to fracture risk [23,24,26]. While macrostructural and densitometric consequences of COVID-19 have begun to be described, its potential influence on the osteocyte lacunar microenvironment remains unexplored. To date, lacunar morphology across Healthy, Osteoporosis, and post–COVID-19 human trabecular bone has not been evaluated within a unified high-resolution and statistically rigorous framework. In a previous study [32], we exploited synchrotron imaging to identify lacunar-level alterations associated with osteoporosis and COVID-19, with a particular focus on micro-damage mechanisms and their relation to mechanical behavior. However, that study was limited by a relatively small sample size and did not explicitly account for the hierarchical structure of lacunae nested within patients. These limitations motivated the present work: here, we address these gaps through large-scale, three-dimensional quantification of osteocyte lacunar morphology in human femoral head trabecular bone across three clinically distinct groups: Healthy, Osteoporosis, and post-

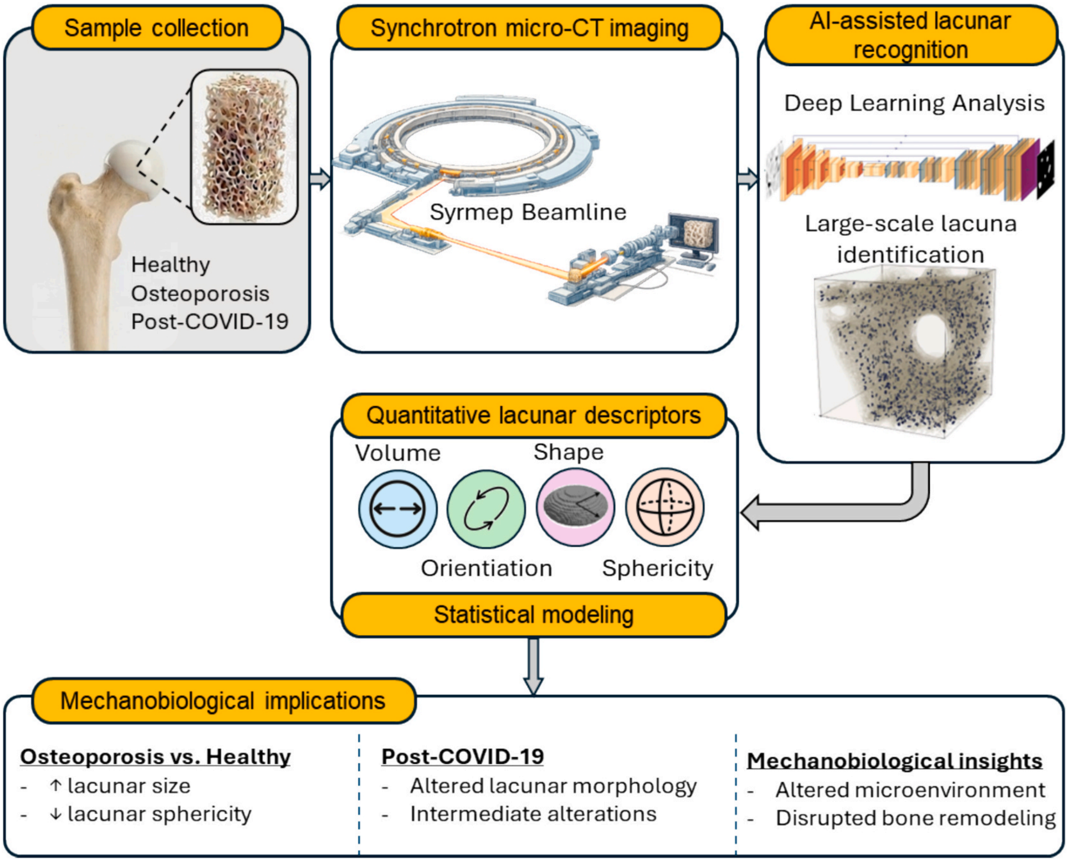

Fig. 1. Workflow for the large-scale analysis of the osteocyte lacunar network in trabecular bone. Trabecular bone samples are first collected from the femoral head and prepared for imaging. High-resolution three-dimensional datasets are then acquired using synchrotron radiation micro–computed tomography (SR-μCT). The reconstructed volumes are processed using artificial intelligence–based methods, such as convolutional neural networks, to automatically detect and segment osteocyte lacunae. From the segmented structures, quantitative morphometric descriptors, including volume, orientation, shape, and sphericity, are extracted. These parameters are subsequently used for statistical modeling to investigate the structural characteristics of the lacunar network and their potential mechanobiological implications.

COVID-19 (Fig. 1). By combining synchrotron phase-contrast imaging with an artificial intelligence-based recognition pipeline, we extracted quantitative morphometric descriptors from approximately 8.96 million lacunae across 48 human specimens, representing one of the largest lacunar datasets reported in human bone to date.

Beyond scale, this work introduces an integrated multilevel statistical framework that explicitly separates lacuna-level effects from patient-level variability, enabling rigorous identification of disease-associated morphometric patterns while accounting for hierarchical data structure. We hypothesize that osteoporotic trabecular bone exhibits a coherent lacunar morphometric shift characterized by altered size, shape, and orientation descriptors relative to healthy bone. As an exploratory objective, we further investigate whether post–COVID-19 bone presents measurable deviations in lacunar microarchitecture compared with healthy or osteoporotic tissue. By integrating sub-micron imaging resolution, automated segmentation, and hierarchical modelling within a single workflow, this study establishes a quantitative benchmark for pathology-associated lacunar remodelling in human trabecular bone and provides structural input for future mechanobiological and multiscale modelling investigations.

2. Materials and methods

2.1. Population set and clinical data

A cross-sectional ex vivo study was conducted on human femoral heads to compare trabecular bone microarchitecture among three clinical groups: Healthy controls, Osteoporosis, and post–COVID-19 patients. All participants were adult women (>18 years) undergoing femoral neck osteotomy as part of primary total hip arthroplasty.

Only female subjects were included to minimize sex-related variability in bone microarchitecture and to reflect the higher prevalence of Osteoporosis in women. Clinical classification was established based on routine preoperative imaging, including computed tomography (CT) and dual-energy X-ray absorptiometry (DXA). Osteoporosis was defined by a T-score ≤ -2.5 according to World Health Organization (WHO) criteria. The post–COVID-19 group included patients with a confirmed SARS-CoV-2 infection (rapid antigenic or RT-PCR testing) who had experienced symptomatic disease within 12 months prior to surgery. Clinical manifestations were heterogeneous and included respiratory, cardiovascular, gastrointestinal, and neuropsychological symptoms, consistent with WHO definitions.

Exclusion criteria comprised other metabolic or genetic bone disorders, bone tumors, prior contralateral hip arthroplasty, or the presence of synthetic implants that could interfere with morphometric analyses.

Femoral heads were collected following approval by the Ethics Committee of San Raffaele Hospital (Milan, Italy; approval date: May 13, 2020; ClinicalTrials.gov ID: NCT04787679). Written informed consent was obtained from all participants. Demographic characteristics and densitometric parameters of the cohort are reported in Section 3.

2.2. Bone samples workflow and pre-scan preparation

Femoral heads (FHs) were fixed in 4% buffered formaldehyde, rinsed thoroughly with deionized water, and stored in 70% ethanol until processing. Each FH was systematically subdivided relative to the coronal plane into three anatomical zones: anterior (Z1), central (Z2), and posterior (Z3). Each zone was further partitioned into proximal (P), medial (M), and distal (D) sub-regions based on spatial orientation with respect to the pelvis, yielding nine anatomically defined sub-regions per specimen. Trabecular samples were primarily harvested from the medial–central (M–Z2) sub-region, corresponding to the principal load-bearing region of the femoral head. Specimens were oriented along the dominant trabecular tension–compression trajectories to ensure representation of mechanically relevant bone architecture, as previously described [27]. From each FH, multiple prismatic trabecular specimens (4 × 4 mm cross-section, 14 mm height) were extracted using a precision diamond saw (Struers ApS Ballerup, Denmark) equipped with a metal-bond diamond cut-off wheel (M0D20; Ø 203 mm, thickness 0.6 mm, Struers, Denmark), suitable for high-hardness mineralized tissues (> HV 800) (Fig. 2A). Following sectioning, samples were rehydrated in phosphate-buffered saline (PBS) to restore physiologically relevant hydration of the collagen–mineral matrix and to optimize phase-contrast imaging conditions prior to synchrotron acquisition.

2.3. Synchrotron micro-CT acquisition and reconstruction

In situ imaging was performed at the SYRMEP beamline of the Elettra Synchrotron, Trieste, Italy, using a propagation-based phase-contrast modality in white-beam configuration, optimized to resolve lacunar-scale features. The sample-to-detector distance was 150 mm, and the X-ray beam, filtered through a 1.5 mm-thick silicon foil, had an effective energy of 25.6 keV, enhancing phase contrast and reducing low-energy artifacts. The samples were scanned in a fly-scan mode, with continuous 360° rotation. Half-acquisition mode was used to double the horizontal field of view via off-center rotation [28]. Projections were acquired using a 16-bit water-cooled Orca Flash 4.0 sCMOS camera (2048 × 2048 pixels) coupled to a 17 μm GGG scintillator, giving a pixel size of 1.6 μm, exposure time of 0.1 s, and 1800 projections per scan over a 3.28 × 3.28 mm^2 field of view. The radiation dose delivered in each scan was ~ 165 Gy, which is well below threshold values for radiation-induced compromise of bone tissue properties (~70 kGy) [29–32].

Data were pre-processed using a single-distance phase-retrieval algorithm [33] with $\delta/\beta = 20 \pm 1$ to enhance the contrast of lacunae and microcracks. Tomographic reconstructions were performed by filtered back-projection using the open-source software SYRMEP Tomo Project (STP) v1.4, designed explicitly for the beamline [34].

A custom MATLAB pipeline was used to clean the reconstructed volumes, following previous works [14,27,32]. This removed noise in inter-trabecular spaces and corrected for scanning artifacts (e.g., ring artifacts, beam hardening), ensuring high-fidelity microstructural features and enabling accurate downstream segmentation of lacunae (Fig. 2B).

2.4. Automated pre-processing and CNN-based lacunar segmentation

SR-microCT volumes exhibit two gray-level distributions, a standard [1] range and an anomalous [-1,0] range caused by acquisition artifacts; to address the low bone-to-background contrast, we apply an automated preprocessing pipeline consisting of min–max normalization, saturation of the lowest and highest 1% of intensities, modality-specific bone masking using Otsu thresholding or K-means clustering, and morphological opening and closing to refine segmentation boundaries. The resulting binary mask suppresses background pixels while preserving bone intensities (Fig. 2C). Fixed-size patches are extracted by sampling $k \times k$ patches with stride s using a sliding-window approach with $k = s = 50$ to comply with GPU memory constraints. Patch selection is guided by bone masks, discarding patches with less than 90% bone tissue and limiting empty patches to at most 30% of each batch.

Segmentation is performed using a deep 2D UNet architecture with an encoder–decoder topology and symmetric skip connections to preserve spatial information across scales [35,36]. In particular, the model consists of four downsampling levels in the encoder and four corresponding upsampling levels in the decoder. At each encoder stage, two consecutive 3 × 3 convolutional layers are applied, followed by batch normalization and ReLU activation, after which the spatial resolution is reduced using 2 × 2 max-pooling. The number of feature channels doubles at each level, starting from 64 filters in the first layer and reaching 512 at the bottleneck. At the bottleneck, two additional 3 × 3 convolutional layers are introduced to increase receptive field depth and improve feature abstraction. In the decoder, upsampling is performed via transposed 2 × 2 convolutions that halve the number of feature

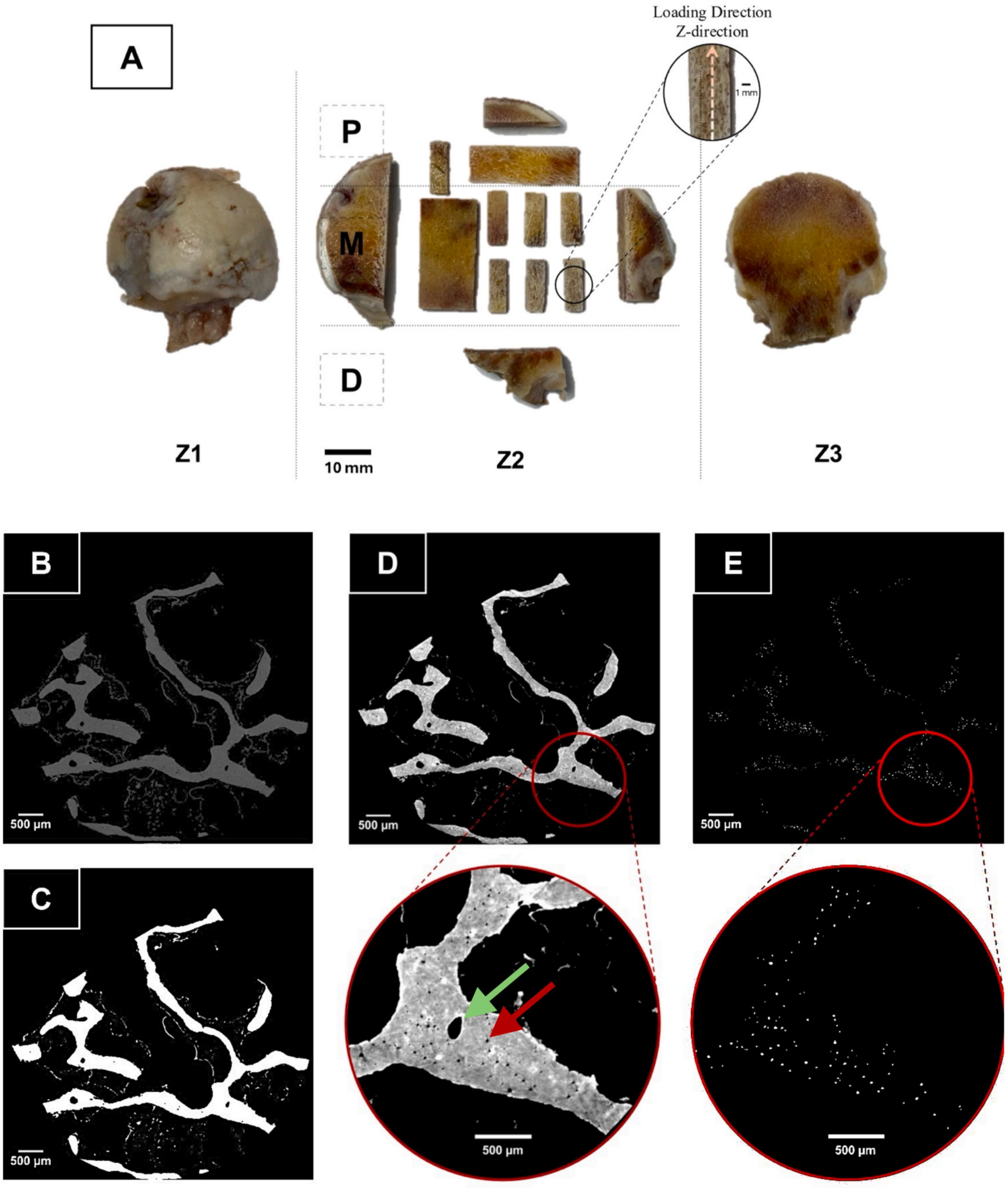

Fig. 2. Preparation of trabecular bone specimens and preprocessing for lacunar segmentation. (A) Representative femoral head from the Healthy group, illustrating the sectioning scheme used to extract multiple trabecular samples (4 × 4 mm cross-section, 14 mm height) from three anatomical zones (Z1–Z3) along the loading (z) direction, including proximal (P), medial (M), and distal (D) regions. (B) Raw reconstructed synchrotron phase-contrast micro-CT slice from an Osteoporosis sample. (C) Corresponding bone mask after Gaussian filtering, Otsu-based thresholding, and morphological operations to isolate trabecular bone. (D) Refined bone region highlighting embedded osteocyte lacunae; the magnified inset below shows lacunae within the trabecular matrix as dark voids shown with the red arrow. The green arrow is showing a vessel. (E) Extracted lacunae from the same Osteoporosis sample after segmentation and filtering, where white spots represent individual lacunae; the magnified inset below details the distribution of segmented lacunae. (For interpretation of the references to colour in this figure legend, the reader is referred to the web version of this article.)

channels and restore spatial resolution. Skip connections concatenate encoder feature maps with decoder ones at matching resolutions to recover fine-grained structural details. Additional convolutional layers are incorporated in the early decoder stages to enhance boundary refinement of lacunar structures. Dropout ($p = 0.3$) is applied after convolutional blocks throughout the network to mitigate overfitting. The final layer consists of a 1 × 1 convolution followed by a sigmoid activation function to produce pixel-wise probability maps. Training is conducted using a combined Binary Cross-Entropy and Dice loss computed on foreground pixels only, encouraging both pixel-level accuracy and overlap maximization. Optimization is performed using the Adam optimizer with an initial learning rate of 0.001, decayed by a factor of 0.7 every 1000 iterations, over a total of 200 epochs (Fig. 3).

This strategy achieves a Dice Similarity Coefficient (DSC) of 63.94 (±4.05) with 99.69% (±0.03) background accuracy for lacunae, demonstrating the potential of the proposed framework as a reliable, automated tool for large-scale bone microarchitecture analysis. Segmentation outputs were further refined by excluding structures outside

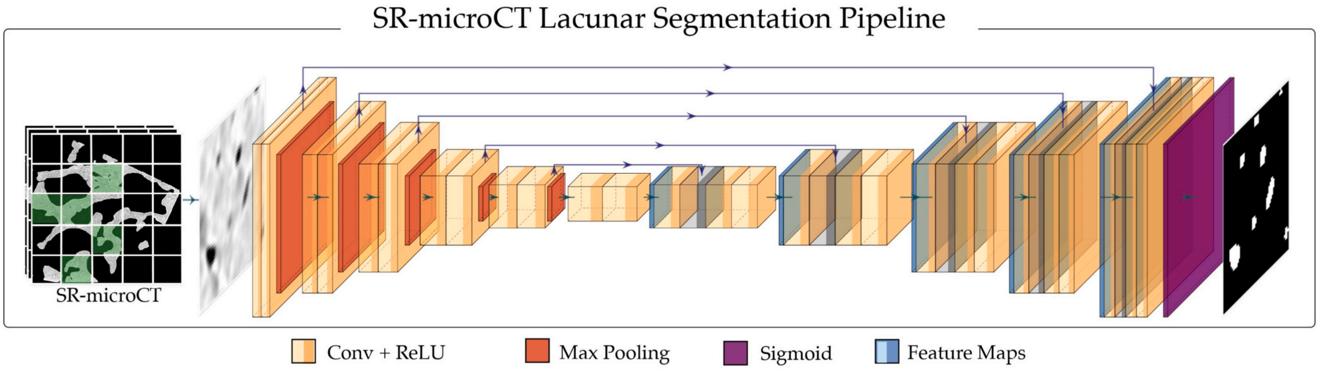

Fig. 3. SR-microCT lacunar segmentation pipeline. SR-microCT volumes are preprocessed using min–max normalization, 1% intensity saturation, modality-specific bone masking (Otsu or K-means), and morphological refinement. Fixed 50 × 50 patches (stride = 50) are extracted, retaining $\geq$ 90% bone content per patch. Segmentation is performed with a 2D U-Net (four encoder–decoder levels with skip connections), using Conv–BatchNorm–ReLU blocks, max pooling, transposed convolutions, and dropout ($p = 0.3$). A final 1 × 1 convolution with sigmoid activation produces probability maps. Training employs combined Binary Cross-Entropy and Dice loss with Adam optimization (initial LR = 0.001, 200 epochs).

the physiological lacunar volume range (400–1229 μm^3, corresponding to 98–300 voxels), consistent with reported values [37] for human osteocyte lacunae in high-resolution imaging studies [17]. The lower threshold was applied to remove segmentation noise and small disconnected artefacts, while the upper threshold was used to exclude larger voids such as microcracks, vascular spaces, or merged lacunar regions that do not represent individual osteocyte lacunae. In addition, elongated non-physiological structures were filtered out to further improve segmentation specificity (Fig. 2D–E). This refinement step ensures that the analyzed dataset is restricted to morphologically and physically plausible lacunae, thereby improving the accuracy and reproducibility of the extracted morphometric descriptors [17].

2.5. Morphometric feature computation and dataset assembly

Morphological features were derived from the lacunar shape tensor obtained from the component-labelled 3D lacunar objects. The following descriptors were calculated (Fig. 4):

i) ***Basic geometric measures.***

Lacunar volume (Lc_Volume) was calculated as the total voxel count

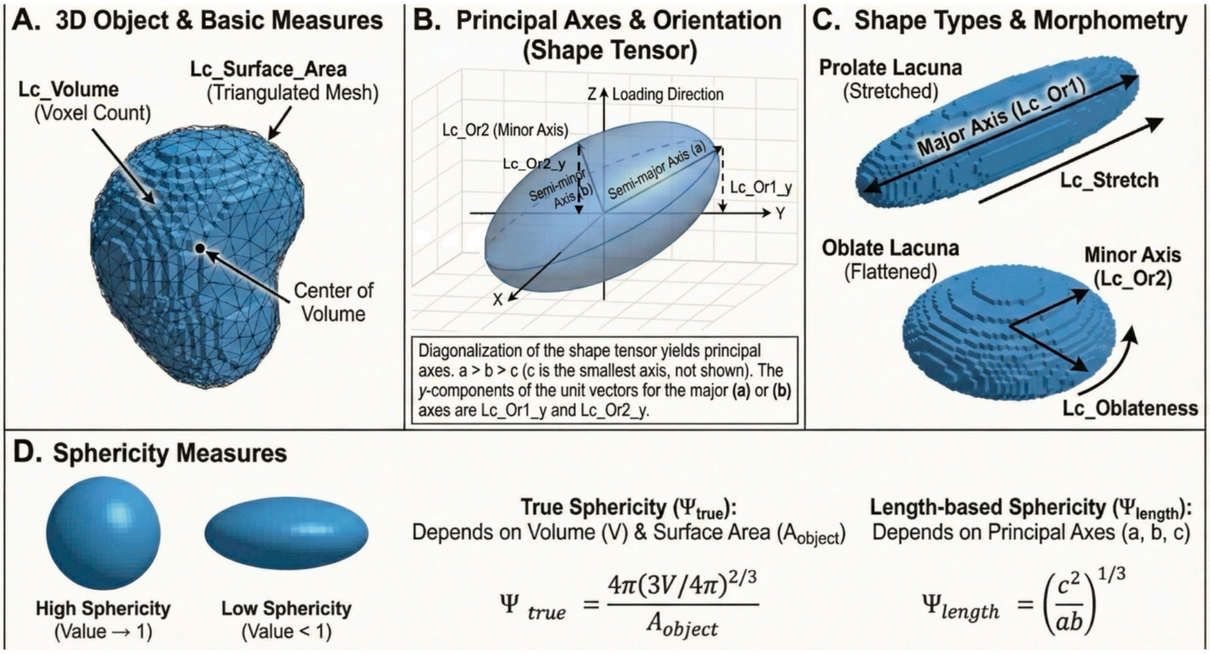

Fig. 4. Schematic representation of lacunar morphometric descriptors derived from the 3D shape tensor. (A) The lacuna is modelled as an ellipsoid obtained by diagonalizing the voxel-based shape tensor [16]. Lacunar volume (Lc_Volume) was calculated as the total voxel count of each segmented lacuna multiplied by the voxel volume, and lacunar surface area (Lc_Surface_Area) was calculated from the triangulated surface mesh generated from the lacunar boundary. (B) From the shape tensor, three orthogonal eigenvectors and corresponding eigenvalues that define the principal axes are obtained. The semi-major axis (a) and semi-minor axes (b) are scaled proportionally to these eigenvalues, where $a > b > c$. Orientation vectors are shown relative to the global coordinate system: Lc_Or1 represents the direction of the semi-major axis, and Lc_Or2 represents the secondary in-plane axis. Component coordinates (e.g., Lc_Or1_y, Lc_Or2_y) illustrate how each orientation projects onto the coordinate system, where we assumed that the z-axis denotes the loading direction. (C) Lacunar Stretch (Lc_Stretch) quantifies overall elongation as the normalized difference between the largest and smallest eigenvalues, and Lacunar Oblateness (Lc_Oblateness) distinguishes rod-like (prolate) from disk-like (oblate) lacunae. (D) For sphericity, the schematic contrasts a nearly spherical lacuna with a more elongated lacuna, emphasizing how reductions in sphericity reflect increased deviation from isotropic shape. True sphericity (Ψ_{true}) depends on lacunar volume and lacunar surface area, while length-based sphericity (Ψ_{length}) depends on principal axes (a, b, c).

of each segmented lacuna multiplied by the voxel volume, and lacunar surface area (Lc_Surface_Area) was calculated from the triangulated surface mesh generated from the lacunar boundary (Fig. 4A) [16].

ii) ***Principal axes and orientation***

Diagonalization of the lacunar shape tensor yields three orthogonal eigenvectors and corresponding eigenvalues ($\lambda_1^2 \leq \lambda_2^2 \leq \lambda_3^2$), which define the principal axes of an equivalent ellipsoid centered at the lacuna. The eigenvalues correspond to the squared semi-axes lengths ($c \leq b \leq a$), while the eigenvectors define their orientations. In this study, two orientation parameters are reported: Lc_Or1, associated with the largest eigenvalue (semi-major axis, a), and Lc_Or2, associated with the intermediate eigenvalue (secondary axis, b). The third principal direction (associated with the smallest eigenvalue, c) is orthogonal to both and is not explicitly reported, as the orientation of the ellipsoid is fully defined by two independent axes [16,38].

Orientation parameters describe only directional information, while axis magnitudes are quantified separately. Each orientation component (e.g., Lc_Or1_y, Lc_Or2_y) represents the projection of the corresponding eigenvector onto a global coordinate system, where the z-axis is aligned with the principal trabecular loading direction and the x–y plane is orthogonal to it, as defined by specimen preparation (Fig. 4B). This procedure defines a consistent right-handed global coordinate system across specimens, based on the extraction axis and cutting geometry. The relative importance of the orientation parameters depends on lacunar geometry. In prolate lacunae ($a \gg b \approx c$), orientation is primarily described by Lc_Or1, reflecting the dominant elongation direction. In contrast, in oblate lacunae ($a \approx b \gg c$), both Lc_Or1 and Lc_Or2 describe the in-plane orientation of the lacuna, while the third axis defines the normal direction to the lacunar plane [16,38].

iii) ***Shape descriptors***.

Additional morphometric features, including Lacunar Stretch (Lc_Stretch) and Lacunar Oblateness (Lc_Oblateness), were computed following established 3D lacunar morphometry definitions (Fig. 4C). Lc_Stretch quantified the degree of elongation as the normalized difference between the largest and smallest eigenvalues,

$$\mathrm{Lc}\backslash\_\mathrm{Stretch} = \frac{\lambda_3 - \lambda_1}{\lambda_3} \tag{1}$$

while Lc_Oblateness characterized whether the lacuna was rod-like (prolate) or plate-like (oblate).

$$\mathrm{Lc}\backslash\_\mathrm{Oblateness} = 2\,\frac{\lambda_2 - \lambda_1}{\lambda_3 - \lambda_1} - 1 \tag{2}$$

iv) ***Sphericity measures***

To further characterize lacunar geometry, true and length-based sphericity were computed to enhance the 3D evaluation of lacunar shape. These two measures capture different geometric attributes of an ellipsoid. Length-based sphericity depends solely on the three principal axes and therefore reflects overall elongation while remaining insensitive to surface irregularities[39]. In contrast, true sphericity incorporates both shape and surface complexity, making it more sensitive to voxel resolution and segmentation noise [39,40].

Lacunar true sphericity (Lc_Sphericity) is derived directly from lacunar volume and lacunar surface area [18]. In contrast, length-based sphericity (Lc_Sphericity_Length) is computed from the three principal axes of the fitted ellipsoid ($a > b > c$) [39] shown in Fig. 4D:

$$\Psi_{\mathrm{true}} = \frac{A_{\mathrm{sphere}}}{A_{\mathrm{object}}} = \frac{4\pi\left(\frac{3V}{4\pi}\right)^{2/3}}{A_{\mathrm{object}}} \tag{3}$$

$$\Psi_{\mathrm{length}} = \left(\frac{c^2}{ab}\right)^{1/3} \tag{4}$$

While values nearing 1 indicate highly spherical lacunae, lower values reveal geometries that have become elongated or flattened. This parameter provides a size-invariant measure of lacunar shape complementary to stretch and oblateness. Following morphometric features, densitometric descriptives were also extracted to describe the broader 3D environment: bone volume fraction (BV/TV), lacunar volume fraction (Lc_Vol/BV), and lacunar number density (Lc_num/BV). Bone volume (BV) was obtained from a bone mask generated through Otsu-based binarization of the reconstructed images. Total volume (TV) was defined as the volume of the enclosing rectangular cube of the bone sample. Total lacunar volume (Lc_Vol) and lacunar count (Lc_num) were derived from the automated segmentation pipeline described previously. Accordingly, all morphological and densitometric metrics were extracted using a validated synchrotron micro-CT processing framework [32] to ensure accuracy and reproducibility across samples.

2.6. *Statistical modelling and multivariate analyses*

Data analysis was performed in Python 3.11, considering the following scientific packages: NumPy v2.2.3, pandas v2.2.3, SciPy v1.15.2, statsmodels v0.14.4, seaborn v0.13.2, pingouin v0.5.5, and matplotlib v3.10.1 in conjunction with IBM SPSS Statistics 26. Given the hierarchical structure of the observations, multilevel modeling was used for analyses. Individual lacunae (Level 1) were nested within patients (Level 2), who were assigned to three clinical groups (Level 3: Healthy, Osteoporosis, post-COVID-19). This structure violates the independence assumption of classical ANOVA; therefore, linear mixed-effects models (LMMs) were required for lacuna-level inference [41–43].

Lacunar-level analysis.

In the preprocessing phase, the Shapiro–Wilk test was used to assess the normality of variable distributions. Outliers were identified using the interquartile range (IQR) rule, which identified values below $Q1 - 1.5 \times \mathrm{IQR}$ or above $Q3 + 1.5 \times \mathrm{IQR}$. Missing values and outliers were removed row-wise.

For each morphometric lacunar feature, a separate LMM was fitted to assess between-group differences while accounting for the nested data structure. The general model form was [44]:

$$Y_{ij} = \beta_0 + \beta_1(\mathrm{Group}_i) + \beta_2(\mathrm{Age}_i) + u_i + \varepsilon_{ij} \tag{5}$$

where Y_{ij} is the lacunar feature for lacuna j in patient i; Group and Age are Level-2 predictors; u_i is a patient-specific random intercept representing between-patient variability; and ε_{ij} is the lacuna-level residual. A random intercept model was selected because both fixed predictors vary only at the patient level, making random slopes unsupported by the data structure. This ensured that group comparisons accounted for both between-patient variation and the strong within-patient similarity of lacunae. Models were fitted using restricted maximum likelihood (REML) with Type III tests of fixed effects. Variance components were extracted to quantify the proportion of total variability attributable to patient-level clustering using Intraclass Correlation Coefficients (ICC) [45]. The ICC values also indicated whether patient-level variance was substantial enough to justify the use of mixed-effects models.

Patient-level analysis.

A liberal screening threshold of $p\text{-value} < 0.20$ was used to identify candidate variables for inclusion in multivariate modelling and to help prevent the exclusion of potentially relevant predictors [46].

Lacunar features were then aggregated for each patient, yielding one representative value per feature, so as to ensure statistical independence of observations. Aggregation was based on variable distribution: normally distributed features were summarized using means, and non-normal features using medians to limit the influence of skewness and outliers. A multivariate general linear model (GLM) was used to test whether the aggregated lacunar morphological profile differed between groups. The clinical group was included as the fixed factor, and age was a covariate. Multivariate significance was evaluated using Pillai's Trace, Wilks' Lambda, Hotelling's Trace, and Roy's Largest Root. When multivariate effects were significant, univariate GLM tests with Bonferroni-adjusted post-hoc comparisons were performed to identify the features contributing most to group differences. Effect-size (η_p^2) and power considerations (μ^2) were also taken into account: large effects can be reliably detected with smaller sample sizes, whereas small effects require larger sample sizes to achieve a statistically meaningful *p*-value < 0.05. For interpretation, effect-size thresholds were defined as small ($\eta_p^2 \approx 0.01$), medium ($\eta_p^2 \approx 0.06$), and large ($\eta_p^2 \approx 0.14$). Patient-level densitometric parameters, measured independently for each patient, were analyzed using a traditional one-way ANOVA with Bonferroni post hoc correction. When Levene's test indicated violation of homogeneity of variances, Welch's ANOVA (Welch's F test) followed by Games–Howell post-hoc tests was used.

3. Results

To determine whether pathology-associated alterations in bone quality are reflected at the lacunar scale, we first characterized patient demographics and global densitometric parameters before proceeding to lacuna-level morphometric analyses. Forty-eight female patients were included, divided into three groups: Healthy, Osteoporosis, and post-COVID-19 (for each group, $n = 16$). Mean age for each subgroup was as follows: Healthy: 72.0 ± 7.4 years; Osteoporosis: 77.8 ± 8.9 years; post-COVID-19: 68.1 ± 14.0 years. A one-way ANOVA revealed a significant difference in age among the groups ($p = 0.013$). Summary statistics for the characteristics of each group, as well as bone volumetric parameters, are shown in Table 1. BV/TV, at the patient level, showed a significant decrease in the Osteoporosis group in comparison to Healthy ($p = 0.019$). Post-COVID-19 presented intermediate values in bone reduction, but not significantly different from healthy groups ($p = 0.136$). Since Levene's test indicated a violation of the homogeneity of variances, Welch's ANOVA/Welch's F test, followed by Games–Howell post-hoc tests, was performed for this parameter. Moreover, the lacunar number density and the lacunar volume fraction did not show differences among the groups.

3.1. *Lacuna-level morphometric differences linear mixed-effects models*

Lacuna-level analyses of 8.96 million lacunae were conducted using linear mixed-effects models that reflect the three-level hierarchical structure of the data. Lacunae were nested within patients nested within clinical groups: Healthy (H), Osteoporosis (O), post-COVID-19 (C). Each model included Group as a fixed effect, age as a covariate, and a random patient-specific intercept estimated using REML and Type III fixed-effect tests, respectively. Results are reported following the LEVEL (Logical Explanations & Visualizations of Estimates in Linear mixed models) approach [44].

Several morphometric parameters showed significant group effects after accounting for age and patient-level clustering, as summarized in Table 2. In the 3D evaluation of lacunar shape results, surface-based sphericity showed a significant global effect of group, $F(2, 44.99) = 4.32$, *p*-value $= 0.019$. healthy samples had higher sphericity than

Table 2
Linear mixed-effects model pairwise comparisons of estimated marginal means for lacunar features with significant Bonferroni-corrected p-values.

Feature	Contrast	Mean Difference* ± SE	(95% CI) **	*p*_value**
Volume (μm^3)	H–O	−39.328 ± 23.520	(−97.817 – 19.162)	n.s.
	H–C	20.009 ± 23.520	(−36.128 – 76.147)	n.s.
	C–O	−59.337 ± 23.520	(−117.827 – −0.848)	**0.046**
Surface Area (μm^2)	H–O	−24.669 ± 11.975	(−54.449 – 5.111)	n.s.
	H–C	7.698 ± 11.975	(−22.082 – 37.478)	n.s.
	C–O	−32.367 ± 11.975	(−62.147 – −2.587)	**0.029**
Semi-Minor Axis (μm)	H–O	−0.144 ± 0.088	(−0.364 – 0.075)	n.s.
	H–C	0.119 ± 0.088	(−0.101 – 0.339)	n.s.
	C–O	−0.263 ± 0.088	(−0.483 – −0.044)	**0.014**
True Sphericity	H–O	0.012 ± 0.004	(0.002 – 0.023)	**0.019**
	H–C	0.004 ± 0.004	(−0.007 – 0.014)	n.s.
	C–O	0.009 ± 0.004	(−0.002 – 0.019)	0.156
Length-Based Sphericity	H–O	0.014 ± 0.006	(−0.001 – 0.028)	0.064
	H–C	−0.001 ± 0.006	(−0.015 – 0.014)	n.s.
	C–O	0.015 ± 0.006	(0.000 – 0.029)	**0.044**
Y-component of the Orientation – minor axis (Lc_Or2_y)	H–O	−0.029 ± 0.010	(−0.055 – −0.003)	**0.024**
	H–C	−0.006 ± 0.010	(−0.032 – 0.020)	n.s.
	C–O	−0.023 ± 0.010	(−0.049 – 0.003)	0.091

p-values > 0.2 are reported as n.s. (not significant) and p-value < 0.05 are bolded;
All models adjust for Age.
[*] Based on the estimated marginal mean;
[**] Bonferroni-adjusted; H = Healthy, O = Osteoporosis, C = post-COVID-19.

Table 1
Group Characteristics and Bone Volumetric Measures.

Feature	Healthy (n = 16) Mean ± SD	Osteoporosis (n = 16) Mean ± SD	Post-COVID-19 (n = 16) Mean ± SD	Comparison	*p*-value
Age (years) **	72.0 ± 7.4	77.8 ± 8.9	68.1 ± 14.0	H–O H–C C–O	**0.014** n.s. **0.010**
BV/TV (%)*	29.15 ± 8.84	21.72 ± 4.87	23.12 ± 8.45	H–O H–C C–O	**0.019** 0.136 n.s.
Lc_Vol/BV**	0.00207 ± 0.00051	0.00243 ± 0.00059	0.00197 ± 0.00075	H–O H–C C–O	n.s. n.s. 0.123
Lacunar Density (Lc_num/BV) [μm^{-3}]	$1.46 \times 10^{-5} \pm 2.84 \times 10^{-6}$	$1.52 \times 10^{-5} \pm 2.43 \times 10^{-6}$	$1.40 \times 10^{-5} \pm 3.54 \times 10^{-6}$	H–O H–C C–O	n.s. n.s. n.s.

p-values > 0.2 are reported as n.s. (not significant) and *p*-value < 0.05 are bolded;
BV/TV: bone volume fraction; Lc_num/BV: lacunar number density; Lc_Vol/BV: lacunar volume fraction; H: Healthy, O: Osteoporosis, C: post-COVID-19.
[*] Welch's ANOVA (Welch's F test) followed by Games–Howell post-hoc tests;
[**] one-way ANOVA with Bonferroni post hoc correction;

Osteoporosis (H–O = 0.012, 95% CI 0.002 to 0.023, *p*-value = 0.019), but contrasts involving post-COVID-19 did not reach significance. Similarly, length-based sphericity showed a significant global group effect, F(2, 44.99) = 4.05, *p*-value = 0.024. The post-COVID-19–Osteoporosis comparison reached significance (C–O = 0.015, 95% CI 0.000 to 0.029, *p*-value = 0.044), while the Healthy–Osteoporosis and Healthy– post-COVID-19 contrasts were not significant.

A significant difference in lacunar shape was also observed between the Osteoporosis and post-COVID-19 groups. Lacunar surface area was significantly different across the groups, F(2, 45) = 3.99, *p*-value = 0.025. The age-adjusted Estimated Marginal Means (EMMs) ± Standard Error (SE) were highest in Osteoporosis (410.12 ± 8.47 μm^2), followed by Healthy (385.45 ± 8.47 μm^2) and post-COVID-19 (377.75 ± 8.47 μm^2). The pairwise contrasts showed that post-COVID-19 exhibited significantly smaller lacunar surface areas than Osteoporosis, C–O = − 32.37 μm^2, 95% CI − 62.15 to − 2.59, *p*-value = 0.029, whereas the Healthy–Osteoporosis and Healthy–COVID-19 comparisons were not significant. EMMs represent group means after accounting for patient-level variability and adjusting for covariates, allowing fair comparisons across groups (Fig. 5A-L).

Group differences were also apparent in the lacunar semi-minor axis length, F(2, 45) = 4.46, *p*-value = 0.017. Osteoporotic lacunae exhibited the largest semi-minor-axis dimensions, and the COVID-19–Osteoporosis contrast confirmed a significant reduction in post-COVID-19 (C–O = − 0.263 μm, 95% CI − 0.483 to − 0.044, *p*-value = 0.014). Differences between Healthy and the remaining groups did not reach significance.

Finally, group differences were also observed for the y-component of the lacunar orientation around the minor axis (Lc_Or2_y), F(2, 45.13) = 4.33, *p*-value = 0.019. Estimated marginal means indicated that Osteoporosis exhibited the highest y-component orientation values (0.141), compared with Healthy (0.112) and post-COVID-19 (0.118). The Healthy–Osteoporosis contrast was significant (H–O = − 0.029, 95% CI − 0.055 to − 0.003, *p*-value = 0.024), and the post-COVID-19–Osteoporosis contrast approached significance (p = 0.091), suggesting a disease-related shift in lacunar alignment. The Healthy– post-COVID-19 contrast was not significant. In addition, a number of features did not demonstrate a significant overall group effect. These included Lc_Stretch, Lc_Oblateness, and the Surface Area to Volume ratio. Semi-major axis and its corresponding orientation exhibited a significant overall group effect; however, neither feature showed significant pairwise differences after correction. Although none of these variables yielded post-hoc contrasts with *p*-value < 0.05, the direction of the fixed-effect estimates remained consistent with the morphological pattern observed in Osteoporosis. Variance decomposition demonstrated that patient-level clustering was very low, with ICCs ranging from 0.002 to 0.087 across parameters (Table 3). ICCs lower than 0.10 indicate that the contribution of between-patient variability to total variance was minimal. In other words, although the methodological justification for using mixed-effects models is preserved, the hierarchical structure of the data had a relatively limited impact on the estimates.

In this context, aggregated statistical modelling is equally defensible. When cluster-level variance is low, summarizing lacunar features at a patient level and analyzing these composites with a multivariate general

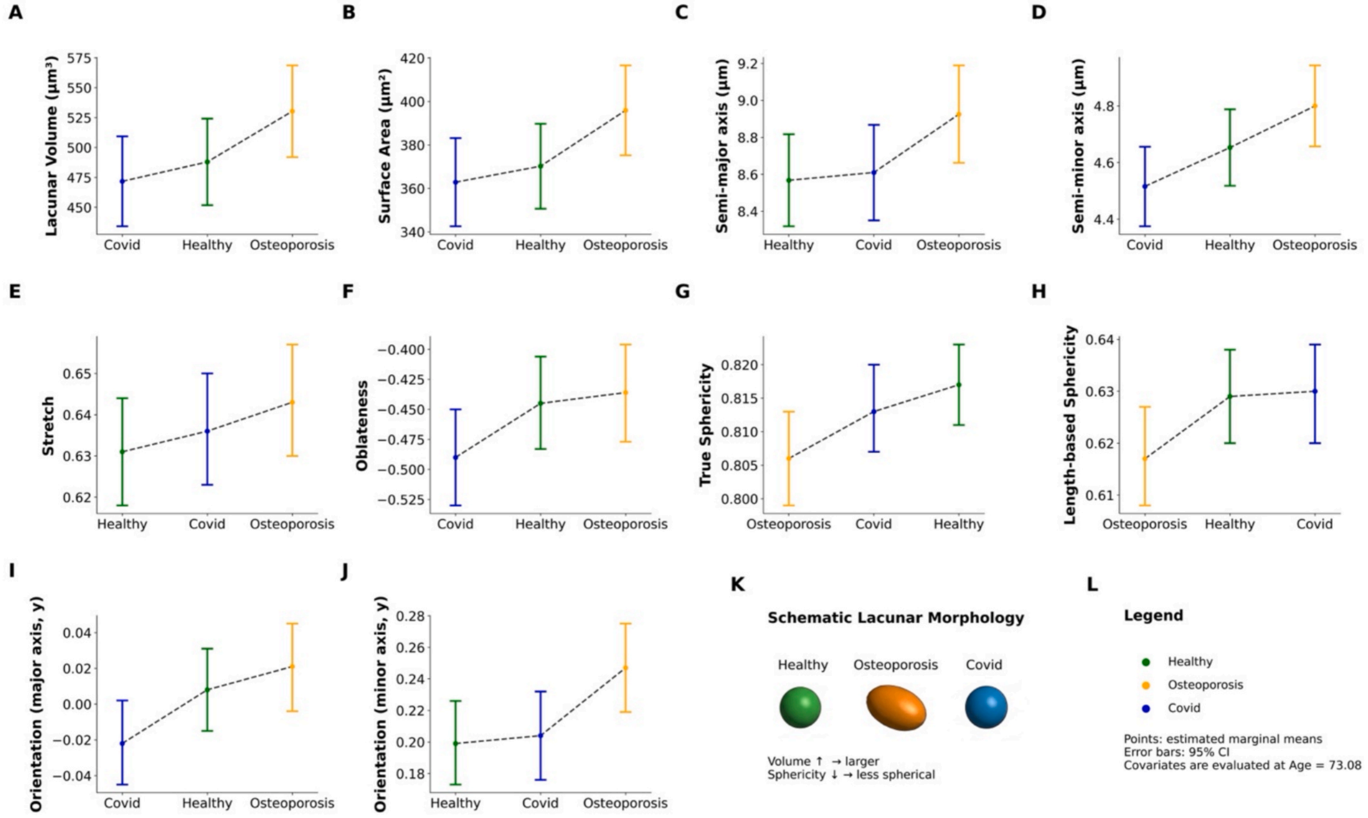

Fig. 5. Estimated marginal means (EMMs) ± 95% confidence intervals for key lacunar morphometric features: Estimated marginal means of osteocyte lacunar morphological descriptors across Healthy, Osteoporosis, and post-COVID-19 groups. Panels show: **(A)** lacunar volume (Lc_Volume), **(B)** surface area (Lc_Surface_Area), **(C)** semi-major axis (semi_Major_Axis), **(D)** semi-minor axis (semi_Minor_Axis), **(E)** stretch (Lc_Stretch), **(F)** oblateness (Lc_Oblateness), **(G)** true sphericity (Lc_Sphericity), **(H)** length-based sphericity (Lc_Sphericity_Length), **(I)** orientation component along the y-axis of the major axis (Lc_Or1_y), and **(J)** orientation component along the y-axis of the minor axis (Lc_Or2_y). Points represent estimated marginal means and error bars indicate 95% confidence intervals obtained from linear mixed-effects models including age as a covariate and patient as a random intercept. The dashed line connects group means to highlight trends across groups. Panel **(K)** provides a schematic illustration of lacunar morphological differences, indicating increased volume and reduced sphericity. Panel **(L)** shows the legend for group color coding. Covariates were evaluated at Age = 73.08.

Table 3

Overall group effect and variance components (LMMs, lacuna-level) for features with p-value < 0.2.

Feature	F(df_1, df_2)	p-value *	σ^2_residual	σ^2_patient	ICC
Volume (μm^3)	F(2, 44.999) = 3.30	**0.046**	49001.58	4425.19	0.083
Surface area (μm^2)	F(2, 45.000) = 3.99	**0.025**	12031.10	1147.17	0.087
Semi-Minor axis (μm)	F(2, 44.999) = 4.46	**0.017**	1.05813	0.06244	0.056
Semi-Major axis (μm)	F(2, 44.995) = 3.56	**0.038**	3.46380	0.22517	0.061
Trues sphericity	F(2, 44.993) = 4.32	**0.019**	0.00267	0.00015	0.053
Length-based sphericity	F(2, 44.985) = 4.05	**0.024**	0.00617	0.00027	0.042
Stretch	F(2, 44.977) = 1.80	0.178	0.01071	0.00053	0.047
Oblateness	F(2, 44.988) = 1.94	0.156	0.14994	0.00379	0.025
Y-component of the Orientation – minor axis (Lc_Or2_y)	F(2, 45.127) = 4.33	**0.019**	0.36809	0.00087	0.002
Y-component of the Orientation – major axis (Lc_Or1_y)	F(2, 44.970) = 2.85	0.068	0.26850	0.00652	0.002

p-values < 0.05 are bolded.

All models adjust for Age.

* Bonferroni-adjusted; σ^2_residual: Residual variance; σ^2_patient: Random intercept variance; ICC = σ^2_patient / (σ^2_patient + σ^2_residual);

linear model, MANOVA, provides a coherent and interpretable multivariate framework. As such, patient-level MANOVA represents a reasonable alternative that complements the lacuna-level LMM results.

3.2. Patient-level multivariate differences

Patient-level analyses were conducted on aggregated lacunar morphology (mean or median values depending on distributional properties). Features were pre-screened using a liberal inclusion threshold ($p < 0.20$), consistent with recommendations to avoid prematurely excluding potentially informative predictors. A multivariate general linear model (MANOVA) with Group as the fixed factor and age as a covariate was applied. Because Box's M test indicated a violation of covariance homogeneity, Pillai's Trace was selected as the more robust statistic. The model revealed a significant overall group effect, Pillai's Trace = 0.680, F(18, 74) = 2.16, p-value = 0.013, partial η2 = 0.340, observed power = 0.965, while age showed no significant multivariate contribution, Pillai's Trace = 0.110, F(9, 36) = 0.496, p-value = 0.868, partial $\eta^2 = 0.110$, observed power = 0.204.

Based on these results, evidence was sufficient to reject the null hypothesis and conclude that lacunar morphology among the 3 clinical groups significantly differed. The observed power was 0.965, indicating that there was a 96.5% chance that the results could have been significant.

Univariate follow-up analyses for pre-screened variables with p-value < 0.20 from the LMM stage are presented in Table 4. Y-component of the Orientation along the major axis (Lc_Or1_y) showed a near-significant group effect, F(2,45) = 3.120, p-value = 0.054, partial $\eta^2 = 0.124$, observed power = 0.571, with Osteoporosis demonstrating the highest alignment values (0.0175 ± 0.0462) relative to the Healthy and post-COVID-19 groups (0.0087 ± 0.0484 and –0.0192 ± 0.0401, respectively). Y-component of the orientation around the minor axis (Lc_Or2_y) reached statistical significance, F(2,45) = 3.399, p-value = 0.042, partial $\eta^2 = 0.134$, observed power = 0.610, again showing elevated values in the Osteoporosis group (0.2489 ± 0.0489) compared with Healthy (0.1991 ± 0.0673) and post-COVID-19 (0.2023 ± 0.0355). Semi-minor axis length also differed significantly across groups, F(2,45) = 3.750, p-value = 0.031, partial $\eta^2 = 0.146$, observed power = 0.656, with Osteoporosis exhibiting the longest axis lengths (4.798 ± 0.332 μm) compared with Healthy (4.653 ± 0.202 μm) and post-COVID-19 (4.518 ± 0.243 μm). True sphericity approached significance, F(2,45) = 2.893, p-value = 0.066, partial $\eta^2 = 0.116$, observed power = 0.537, again reflecting lower values in the Osteoporosis group (0.8045 ± 0.0149) relative to Healthy (0.8172 ± 0.0092) and post-COVID-19 (0.8147 ± 0.0129).

Partial η^2 values between 0.108 and 0.146 reflect effects of moderate magnitude, approaching the conventional threshold for large effects. These values indicate that the analyses were able to detect group differences of meaningful size. The convergence of significant effects across multiple shape descriptors suggests robust morphological signatures.

Results for pairwise comparisons (Table 5) indicated various near-significant comparisons after Bonferroni correction, particularly for the Osteoporosis group. In terms of the y-component of orientation features, the difference between the major axis and the semi-minor axis for Healthy–Osteoporosis and post-COVID-19–Osteoporosis was nearly significant, indicating a trend towards increasing alignment in Osteoporosis. The semi-major axis length showed a significant difference between the post-COVID-19 and Osteoporosis groups ($p = 0.027$), with the Osteoporosis group exhibiting larger values. The true sphericity had a near-significant difference between the Healthy and Osteoporosis groups ($p = 0.064$), denoting lower values for the Osteoporosis group.

The finding of significant effects for multiple characteristics together provides a clear lacunar morphological pattern for the disease, as reported in Fig. 6, where the normalized lacunar morphology profile plot is shown with 95% confidence intervals.

Table 4

Univariate Effects of Group on Lacunar Morphology for prescreened features with p-value < 0.2 from LMM analyses p-values > 0.2 are reported as n.s. (not significant) and p-value < 0.05 are bolded; *Bonferroni-adjusted; H = Healthy, O = Osteoporosis, C = post-COVID-19, Lc_Or1_y: y-component of the Orientation – major axis, Lc_Or2_y: y-component of the Orientation – minor axis.All models adjust for Age.

Feature	H: Mean ± SD	O: Mean ± SD	C: Mean ± SD	F(2,45)	p-value*	Partial η^2	Observed Power
Stretch	0.6302 ± 0.0244	0.6463 ± 0.0261	0.6340 ± 0.0263	0.910	n.s.	0.040	0.197
Oblateness	−0.4442 ± 0.0657	–0.4392 ± 0.0700	–0.4877 ± 0.0879	2.040	0.142	0.085	0.398
Lc_Or1_y	0.0087 ± 0.0484	0.0175 ± 0.0462	–0.0192 ± 0.0401	3.120	0.054	0.124	0.571
Lc_Or2_y	0.1991 ± 0.0673	0.2489 ± 0.0489	0.2023 ± 0.0355	3.399	**0.042**	0.134	0.610
Surface Area (μm^2)	370.11 ± 21.42	396.48 ± 46.25	362.39 ± 42.40	2.659	0.081	0.108	0.501
Semi-Major Axis (μm)	8.560 ± 0.304	8.969 ± 0.508	8.574 ± 0.616	2.156	0.128	0.089	0.418
Semi-Minor Axis (μm)	4.653 ± 0.202	4.798 ± 0.332	4.518 ± 0.243	3.750	**0.031**	0.146	0.656
Length-Based Sphericity	0.6290 ± 0.0161	0.6151 ± 0.0201	0.6314 ± 0.0169	2.045	0.142	0.085	0.399
True Sphericity	0.8172 ± 0.0092	0.8045 ± 0.0149	0.8147 ± 0.0129	2.893	0.066	0.116	0.537

Table 5
Pairwise Comparisons for features with significant or near-significant group differences in MANOVA.

Feature	Contrast	Mean Diff* ± SE	*p*-value**	95% CI
Y-component of the Orientation – major axis (Lc_Or1_y)	H – O	–0.012 ± 0.017	n.s.	–0.054 to 0.029
	H – C	0.030 ± 0.016	n.s.	–0.011 to 0.070
	C – O	–0.042 ± 0.018	0.063	–0.086 to 0.002
Y-component of the Orientation – minor axis (Lc_Or2_y)	H – O	–0.048 ± 0.019	0.055	–0.096 to 0.001
	H – C	–0.004 ± 0.019	n.s.	–0.051 to 0.043
	C – O	–0.043 ± 0.020	n.s.	–0.094 to 0.008
Semi-Minor Axis (μm)	H – O	–0.148 ± 0.099	n.s.	–0.393 to 0.098
	H – C	0.137 ± 0.096	n.s.	–0.101 to 0.376
	C – O	–0.285 ± 0.104	**0.027**	–0.543 to –0.026
Sphericity	H – O	0.011 ± 0.005	0.064	0.000 to 0.022
	H – C	0.003 ± 0.004	n.s.	–0.008 to 0.015
	C – O	–0.007 ± 0.005	n.s.	–0.020 to 0.005

p-values > 0.2 are reported as n.s. (not significant) and p-value < 0.05 are bolded.
All models adjust for Age.
[*] Mean difference = (I – J); Mean Difference is computed as the mean of group (I) minus the mean of group (J), where positive values indicate higher values in (I) and negative values indicate higher values in (J).
[**] Bonferroni-adjusted; H = Healthy, O = Osteoporosis, C = post-COVID-19.

Patient-level lacunar morphology metrics were Z-normalized across the full groups for each feature (Lc_Volume, Lc_Sphericity, semi_Major_Axis, semi_Minor_Axis, Lc_Stretch, Lc_Oblateness, Lc_Or1, Lc_Or2) to allow comparison across variables with different physical units and scales. Lines represent group means for Healthy (green), Osteoporosis (orange), and post-COVID-19 (blue), with shaded ribbons indicating 95% confidence intervals (mean ± 1.96 × SEM). Values above zero indicate group means higher than the overall cohort average for that feature, whereas values below zero indicate lower-than-average values. The profile highlights a distinct osteoporotic fingerprint characterized by reduced sphericity and increased volume, axis lengths, oblateness, and orientation, compared with the Healthy and post-COVID-19 groups. In addition, Fig. 7 showed a heatmap of Z-normalized lacunar morphology by group. Each cell represents the Z-normalized group means for a given lacunar morphology feature (columns) and clinical group (rows: Healthy, Osteoporosis, post-COVID-19). Normalization was performed across all patients for each feature, such that zero corresponds to the overall cohort mean and ± 1 corresponds to one standard deviation above or below the mean. Osteoporosis shows a coherent pattern of increased volume, axis lengths, oblateness, and orientation (warm colors) accompanied by reduced sphericity (cool colors), whereas the Healthy and post-COVID-19 groups cluster closer to the multivariate baseline.

In aggregate, the above findings reveal that descriptors based on shape and orientation, especially the lengths of the axes and the lacunar sphericity, are the most effective means of distinguishing between the Osteoporosis, Healthy, and post-COVID-19 groups.

4. Discussion

Osteocyte lacunae are central to bone mechanosensing, yet human evidence linking pathology to consistent lacunar alterations remains limited. To our knowledge, this study provides one of the largest and most systematically analyzed three-dimensional datasets of osteocyte lacunar morphology in human trabecular bone, integrating sub-micron synchrotron imaging, AI-driven segmentation, and hierarchical statistical modeling within a single analytical framework. In this cross-sectional study, trabecular bone from human femoral heads of Healthy, Osteoporosis, and post-COVID-19 patients was analyzed using synchrotron micro-CT, AI-based segmentation, and multilevel statistical modeling to characterize pathology-related microstructural changes. Importantly, building upon our previous work [32], this study provides

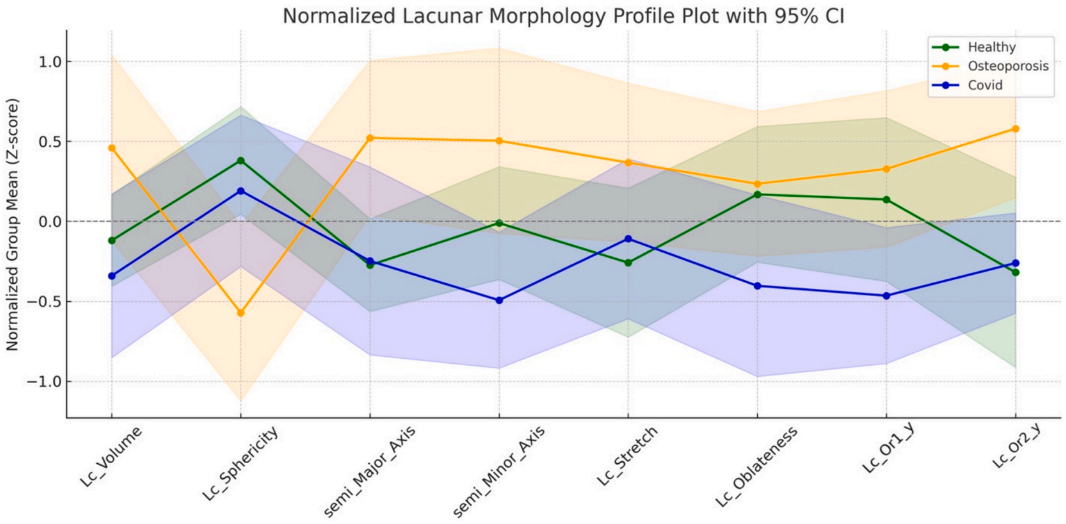

Fig. 6. Normalized lacunar morphology profile plot with 95% confidence intervals. Patient-level lacunar morphology metrics were Z-normalized across the full cohort for each feature (Lc_Volume, Lc_Sphericity, semi_Major_Axis, semi_Minor_Axis, Lc_Stretch, Lc_Oblateness, Lc_Or1, Lc_Or2) to allow comparison across variables with different physical units and scales. Lines represent group means for Healthy (green), Osteoporosis (orange), and post-COVID-19 (blue), with shaded ribbons indicating 95% confidence intervals (mean ± 1.96 × SEM). Values above zero indicate group means higher than the overall cohort average for that feature, whereas values below zero indicate lower-than-average values. The profile highlights a distinct osteoporotic fingerprint characterized by reduced sphericity and increased volume, axis lengths, oblateness, and orientation, compared with the Healthy and post-COVID-19 groups. (For interpretation of the references to colour in this figure legend, the reader is referred to the web version of this article.)

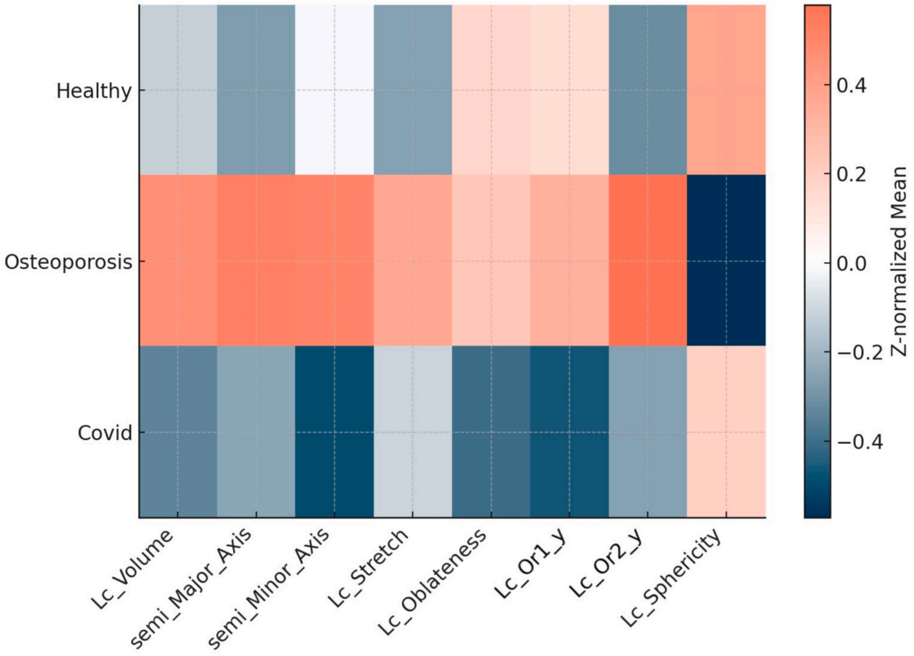

Fig. 7. Heatmap of Z-normalized lacunar morphology by group. Each cell represents the Z-normalized group mean for a given lacunar morphology feature (columns) and clinical group (rows: Healthy, Osteoporosis, post-COVID-19). Normalization was performed across all patients for each feature, such that zero corresponds to the overall cohort mean and ± 1 corresponds to one standard deviation above or below the mean. Osteoporosis shows a coherent pattern of increased volume, axis lengths, oblateness, and orientation (warm colors) accompanied by reduced sphericity (cool colors), whereas the Healthy and post-COVID-19 groups cluster closer to the multivariate baseline.

the first large-scale and statistically rigorous comparison of osteoporotic and post–COVID-19 lacunar microarchitecture in human trabecular femoral head tissue, enabled by an expanded cohort (~8.96 million lacunae) and hierarchical analytical framework.

Compared with post-COVID-19 bone, Osteoporosis was associated with larger lacunae, as indicated by increased lacunar volume, surface area, and semi-minor axis length (p-value < 0.05), with healthy bone showing intermediate values. These size increases were accompanied by a significantly reduced lacunar sphericity in Osteoporosis relative to healthy individuals. Lacunar orientation was also significantly altered in Osteoporosis relative to Healthy, and showed borderline separation from post-COVID-19. At the patient level, MANOVA confirmed a significant overall group effect, mainly driven by semi-minor axis length and near-significant sphericity, with the lowest sphericity in Osteoporosis. The observed power (0.965) indicated high sensitivity to detect multivariate differences. At the patient level, Osteoporosis displayed a significant reduction in BV/TV compared to the healthy counterpart. Importantly, these findings define distinct lacunar morphological fingerprints across the three conditions.

Existing evidence supports the view that stress amplification around osteocyte lacunae is a key mechanical feature shaping osteocyte mechanobiology, as it affects how osteocytes sense loading and transduce mechanical inputs into biochemical signals [8,15,18,21,47]. In the present study, Osteoporosis is associated with a significantly larger volume than post-COVID-19 group. Based on Hemmatian et al., larger lacunae can increase peak effective strains on osteocyte cells relative to smaller cavities [8]. In parallel, Akhter et al. indicated that bone regions with a low-turnover remodeling rate are associated with larger lacunae and reduced lacunar density [18]. Less spherical lacunae, which have been found in the Osteoporosis group, indicate anisotropic cavities that can distort the local strain field around the osteocyte, resulting in higher maximum effective strains on osteocyte cells relative to more equant cavities [8]. These findings indicate two distinct pathology-associated lacunar morphometric patterns.

Although sphericity is a useful size-invariant descriptor of global shape, it is sensitive to image resolution and segmentation quality, which can influence absolute values and their mechanobiological interpretation. To reduce this potential source of bias, we complemented true sphericity (lacunar surface-area relative to a sphere of the same volume) with length-based sphericity. Length-based sphericity captures overall compactness (i.e., how elongated or flattened a lacuna can be) and is relatively insensitive to surface irregularities, whereas true sphericity (commonly reported in prior studies) decreases with edge-like features and is sensitive to imaging resolution [39].

Herein, these data reinforce the relationship between lacunar shape and mechanical environment in Osteoporosis. In Fig. 8, a scatter plot of lacunar volume (Lc_Volume) versus lacunar sphericity (Lc_Sphericity) for Healthy, Osteoporosis, and post-COVID-19 cohorts, illustrating the joint distribution of lacunar size and shape, is shown. The Osteoporosis group is shifted toward larger volumes and lower sphericity, whereas the Healthy and post-COVID-19 groups largely overlap, indicating similar volume–sphericity profiles.

In addition to lacunar shape, lacunar orientation, commonly defined relative to the principal loading axis, modulates the mechanical microenvironment experienced by osteocytes. In long bones, lacunae are typically aligned with the longitudinal axis and tend to follow the predominant collagen fiber orientation [15]. Finite element analyses have demonstrated that deviations from the principal loading direction amplify effective strains and expand the volume of highly strained *peri*-lacunar tissue [48]. Consistently, Hemmatian et al. [8] reported increased peak effective strains in lacunae misaligned with the bone longitudinal axis, highlighting orientation as a determinant of mechanosensitivity.

While prior literature suggests that global lacunar alignment remains relatively stable with aging or disease [6], our results indicate more subtle orientation-dependent alterations. No significant between-group differences were detected in the z-component, corresponding to the nominal loading direction. However, significant differences emerged in the y-component of the minor axis in Osteoporosis compared with Healthy bone, with borderline separation from the post-COVID-19

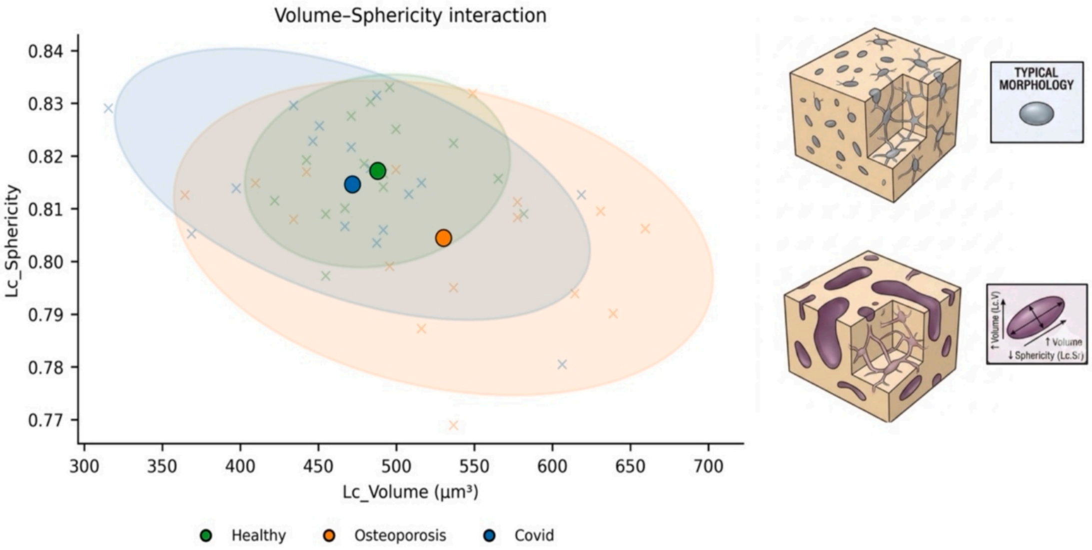

Fig. 8. Volume–sphericity interaction of osteocyte lacunae across study groups. Scatter plot of lacunar volume (Lc_Volume) versus lacunar true sphericity (Lc_Sphericity) for Healthy, Osteoporosis, and post-COVID-19 cohorts. Individual markers (lighter shades) represent patient-level aggregated values, while filled circles (darker shades) indicate group means. Shaded ellipses depict the covariance of each group in the two-parameter space, illustrating the joint distribution of lacunar size and shape. The Osteoporosis group is shifted toward larger volumes and lower sphericity, whereas the Healthy and post-COVID-19 groups largely overlap, indicating similar volume–sphericity profiles.

group. This transverse-plane reorientation may alter how mechanical loads are distributed along the lacunar wall, potentially interacting with the observed increases in lacunar size and anisotropy. Such coordinated modifications in shape and orientation suggest remodeling-driven reorganization of the *peri*-lacunar mechanical niche rather than isolated geometric variability.

Osteocyte lacunar morphology is known to vary with age, hormonal status, anatomical site, and pathology [18,34,49]. Although age differed significantly among groups, it was included as a covariate in all inferential models and did not emerge as a significant determinant of lacunar morphology in multivariate analyses. The cohort consisted exclusively of postmenopausal women (mean age 73.1 ± 11.1 years), reducing hormonal heterogeneity [50]. Furthermore, all specimens were harvested from the same medial–central region of the femoral head (Z2-M), minimizing site-dependent architectural variability. These controls support the interpretation that the observed morphometric differences are primarily associated with pathological condition rather than age, hormonal status, or anatomical location.

Our findings align with prior studies describing pathology-related lacunar alterations [18,32,51], though the literature remains heterogeneous. For example, Goff et al. [21] reported no significant lacunar differences in idiopathic osteoporosis based on transiliac crest biopsies but identified an inverse correlation between BV/TV and lacunar sphericity. It should be noted, however, that the anatomical site differs from the present study, which focuses on trabecular bone from the femoral head. These regions are characterized by distinct mechanical loading environments and remodeling dynamics, which are known to influence bone microarchitecture. Therefore, site-specific factors may contribute to the apparent discrepancies in lacunar alterations reported across studies.

In the present study, Osteoporosis was characterized by both reduced BV/TV and significantly decreased true sphericity, alongside increases in lacunar volume and semi-minor axis length. Compared with post-COVID-19 bone, Osteoporosis demonstrated larger and less spherical lacunae, while Healthy bone consistently exhibited intermediate values. Multivariate analysis confirmed that the semi-minor axis remained significantly elevated in Osteoporosis relative to C post-OVID-19, reinforcing the presence of a distinct geometry-driven shift. Collectively, these findings indicate coordinated alterations in lacunar size and shape in Osteoporosis, whereas post–COVID-19 bone exhibits a partially overlapping but comparatively moderate morphometric profile. The biological implications of these differences warrant further mechanistic investigation.

From a ***biological perspective***, osteocyte lacunar morphology is not only a structural feature but also reflects the dynamic interaction between osteocytes and their surrounding matrix. Osteocytes are capable of modifying the perilacunar matrix through osteocytic osteolysis, a process that is regulated by hormonal and metabolic factors. In osteoporosis, increased bone turnover and estrogen deficiency are associated with dysregulation of this process, potentially leading to enlargement of lacunar spaces and alterations in shape. Such changes may reflect an impaired balance between bone resorption and formation at the cellular level, and may contribute to altered mechanosensitivity and bone quality.

In contrast, the absence of consistent and statistically significant alterations in the post–COVID-19 group suggests that the impact of COVID-19 on bone microarchitecture may be more subtle or indirect. Current evidence indicates that COVID-19 can influence bone metabolism through systemic inflammation, altered cytokine signaling, and reduced physical activity [23,24,26]. However, these effects may not necessarily translate into detectable changes in lacunar morphology within the time frame considered, or may be masked by inter-individual variability related to disease severity and treatment. Further studies integrating clinical, molecular, and microstructural analyses will be required to elucidate the mechanisms underlying bone alterations in post–COVID-19 conditions.

From a ***clinical perspective***, fracture risk represents the primary outcome of interest in osteoporosis and could be relevant also in post-COVID-19 condition too. Although the present study does not include longitudinal clinical outcomes, the identified lacunar morphometric alterations may have direct implications for bone fragility at multiple scales. In particular, increased lacunar volume and reduced sphericity are expected to modify local stress concentration factors and strain amplification within the perilacunar matrix, leading to more heterogeneous stress distributions and a higher propensity for microdamage initiation under physiological loading conditions. At the tissue level, these alterations may contribute to reduced fracture toughness and damage resistance, mechanisms that are not captured by bone mineral density alone. This is consistent with clinical evidence showing that a substantial proportion of fragility fractures occur in patients with non-osteoporotic BMD values, highlighting the importance of microstructural determinants of bone quality [5,11]. In this context, lacunar morphometric descriptors may provide complementary information on the mechanical competence of bone tissue by reflecting the structural state of the osteocyte network and its local mechanical environment. While further validation is required, particularly through studies integrating imaging-derived lacunar descriptors with clinical outcomes such as fracture incidence and patient-specific risk models (e.g., FRAX-based assessment), these findings support the potential role of lacunar morphometry as a complementary biomarker for improving fracture risk stratification beyond conventional densitometric measures.

This study advances prior work by providing large-scale, three-dimensional quantification of lacunar morphology in human trabecular bone across clinically defined cohorts. The balanced design ($n = 16$ per group) and analysis of approximately 8.96 million lacunae across 48 femoral heads provide statistical robustness rarely achievable in human ex vivo studies. AI-based recognition enabled standardized, high-throughput feature extraction, minimizing observer bias and ensuring consistency across specimens. Importantly, this represents one of the first direct structural comparisons of post–COVID-19 and osteoporotic trabecular bone at the lacunar level.

The multilevel statistical framework accounted for the hierarchical structure of lacunae nested within patients. Intraclass correlation coefficients indicated modest clustering effects, supporting the appropriateness of mixed-effects modeling while also demonstrating that aggregated patient-level analyses remain statistically robust. This dual-level approach strengthens confidence in the identified group differences.

However, some limitations should be acknowledged.

First, the present study focuses on single-lacuna morphometric descriptors (size, shape, and orientation), while the spatial organization of the lacunar network, such as inter-lacunar spacing, clustering, and anisotropic distribution, was not explicitly assessed. The quantitative characterization of spatial descriptors in trabecular bone is inherently challenging, as it requires the definition of spatial neighborhoods within finite and structurally heterogeneous volumes and is highly sensitive to boundary effects, sampling variability, and discontinuities associated with trabecular porosity. In particular, distance-based and correlation-based metrics may be biased by irregular geometries and void spaces. In contrast, object-level descriptors can be robustly extracted and compared across large datasets, providing a statistically stable basis for morphometric analysis. Future work will extend the present framework to incorporate spatial statistics and network-based approaches, enabling a more comprehensive characterization of the lacunocanalicular system.

Second, orientation measurements depend on specimen alignment; minor deviations during sample preparation may introduce additional variability when relating orientation components to the nominal loading direction.

Third, synchrotron phase-contrast imaging is resource-intensive, which constrains the number of specimens that can be analyzed, despite the large number of lacunae quantified per sample.

Finally, limitations related to cohort composition should be considered. Osteopenic bone was not included, restricting the investigation across the full continuum of bone fragility. In addition, the post–COVID-19 cohort was not stratified by disease severity or treatment history, which may contribute to within-group variability. The study also includes only female subjects. While this choice reduces biological variability and reflects the higher prevalence of osteoporosis in women, particularly in the context of postmenopausal estrogen deficiency and its effects on bone remodeling, it limits the generalizability of the findings across sexes. Sex-specific differences in bone architecture, remodeling dynamics, and hormonal regulation may influence osteocyte lacunar morphology and its mechanobiological response. These differences may extend to the lacunocanalicular network, potentially affecting lacunar size, shape, and orientation descriptors. Therefore, the morphometric signatures identified in this study should be interpreted within the context of a female cohort. Future investigations including male subjects and more diverse populations will be essential to determine whether these patterns are conserved across sexes or exhibit sex-specific characteristics, thereby enhancing the general applicability of lacunar morphometry as a biomarker of bone quality.

Herein, the present findings demonstrate that pathology-associated alterations in trabecular bone are detectable at the lacunar scale and are characterized predominantly by geometric remodeling rather than changes in lacunar density. Future work will integrate histological assessment of bone tissue age and finite element modeling to determine how the observed alterations in lacunar size, shape, and orientation influence *peri*-lacunar strain amplification and fluid–shear patterns. Such integrative approaches will clarify whether lacunar morphometry can serve as a structural biomarker of disease-specific remodeling dynamics and osteocyte mechanoregulation.

5. Conclusion

This study establishes a large-scale, quantitative three-dimensional characterization of osteocyte lacunar morphology in human trabecular bone. Using a balanced design comprising Healthy, Osteoporosis, and post–COVID-19 cohorts ($n = 16$ per group), we analyzed approximately 8.96 million osteocyte lacunae across 48 femoral head specimens—achieving a scale and statistical robustness rarely attainable in human bone research. AI-based segmentation enabled standardized, automated extraction of lacunar morphometric descriptors from high-resolution synchrotron datasets, ensuring consistency across samples. To our knowledge, this work provides one of the first direct structural comparisons between post–COVID-19 and osteoporotic trabecular bone at the lacunar level. Osteoporosis was characterized by significantly larger lacunae compared with post-COVID-19 ($p < 0.05$), with increases in lacunar volume, surface area, and semi-minor axis length, accompanied by reduced sphericity. Healthy bone exhibited intermediate values. These coordinated changes indicate a geometry-driven remodeling of the *peri*-lacunar microenvironment rather than alterations in lacunar density. A multilevel statistical framework was implemented to account for the hierarchical structure of lacunae nested within patients, enabling rigorous inference at both lacuna and patient levels. Intraclass correlation analysis demonstrated modest clustering effects, supporting the methodological validity of mixed-effects modeling while indicating that patient-level aggregation remains statistically robust for group comparisons.

Herein, this large-scale human study demonstrates that Osteoporosis and post–COVID-19 conditions are associated with quantifiable alterations in lacunar microarchitecture. These findings provide a structural benchmark for disease-associated lacunar remodeling and lay the groundwork for future mechanobiological investigations of how systemic conditions reshape the osteocyte mechanical niche.

CRediT authorship contribution statement

Seyedeh Fahimeh Hosseini: Writing – original draft, Validation, Methodology, Investigation, Formal analysis, Data curation, Conceptualization. **Isabella Poles:** Writing – review & editing, Validation, Resources, Methodology. **Eleonora D'Arnese:** Writing – review & editing, Validation, Resources, Methodology. **Barbara Canciani:** Writing – review & editing, Resources. **Laura Maria Vergani:** Writing – review & editing, Validation, Supervision, Resources, Methodology, Investigation, Funding acquisition, Conceptualization. **Federica Buccino:** Writing – review & editing, Validation, Resources, Methodology, Investigation, Funding acquisition, Conceptualization.

Declaration of competing interest

The authors declare that they have no known competing financial interests or personal relationships that could have appeared to influence the work reported in this paper.

Acknowledgments

The authors acknowledge that the presented work was realized using the infrastructure provided by the Euro-BioImaging initiative https://www.eurobioimaging.eu/https://www.eurobioimaging.eu/

S.F.H., F.B and L.M.V. acknowledge the financial support from the European Union Horizon Europe research and innovation programme under the Marie Skłodowska-Curie (MSCA) grant agreement No 101120290 (GAP).

F.B. and L.M.V. acknowledge Prof. M. D. Santambrogio for the support in the definition of the AI-assisted framework.

The authors acknowledge Prof. L. Zagra and Prof. L. Mangiavini from IRCCS Ospedale Galeazzi-Sant'Ambrogio (Milan, Italy) for providing the femoral heads and support in the preparation of the bone samples.

Data availability

Data will be made available on request.

References

[1] S. Dragoun Kolibová, E.M. Wölfel, H. Hemmatian, P. Milovanovic, H. Mushumba, B. Wulff, M. Neidhardt, K. Püschel, A.V. Failla, A. Vlug, A. Schlaefer, B. Ondruschka, M. Amling, L.C. Hofbauer, M. Rauner, B. Busse, K. Jähn-Rickert, Osteocyte apoptosis and cellular micropetrosis signify skeletal aging in type 1 diabetes, Acta Biomater. 162 (2023) 254–265, https://doi.org/10.1016/j.actbio.2023.02.037.

[2] C.E. Jones, S. Blouin, E. Raguin, R. Weinkamer, A. Berzlanovich, P. Fratzl, M. A. Hartmann, The human osteocyte lacunocanalicular network structure in osteons of the iliac crest of elderly women depends on mineral content but not individual age, Acta Biomater. (2025), https://doi.org/10.1016/j.actbio.2025.11.036.

[3] T. Tang, J. Zhong, J. Hu, V. Schemenz, A. Davydok, R. Brunner, J. Zhou, W. Wagermaier, A.A. Pitsillides, W.J. Landis, P. Fratzl, J. Chen, Gradients in lacunar morphology and cartilage mineralization reflect the mechanical function of the mouse femoral head epiphysis, Acta Biomater. 201 (2025) 385–399, https://doi.org/10.1016/j.actbio.2025.06.002.

[4] J. Klein-Nulend, A.D. Bakker, R.G. Bacabac, A. Vatsa, S. Weinbaum, Mechanosensation and transduction in osteocytes, Bone 54 (2013) 182–190, https://doi.org/10.1016/j.bone.2012.10.013.

[5] P.R. Buenzli, N.A. Sims, Quantifying the osteocyte network in the human skeleton, Bone 75 (2015) 144–150, https://doi.org/10.1016/j.bone.2015.02.016.

[6] W. Sang, A. Ural, Influence of Osteocyte Lacunar-Canalicular Morphology and Network Architecture on Osteocyte Mechanosensitivity, Curr. Osteoporos. Rep. 21 (2023) 401–413, https://doi.org/10.1007/s11914-023-00792-9.

[7] J.U.A. Choi, A.W. Kijas, J. Lauko, A.E. Rowan, The Mechanosensory Role of Osteocytes and Implications for Bone Health and Disease States, Front. Cell Dev. Biol. 9 (2022), https://doi.org/10.3389/fcell.2021.770143.

[8] H. Hemmatian, A.D. Bakker, J. Klein-Nulend, G.H. van Lenthe, Alterations in osteocyte lacunar morphology affect local bone tissue strains, J. Mech. Behav. Biomed. Mater. 123 (2021), https://doi.org/10.1016/j.jmbbm.2021.104730.

[9] S. von Kroge, J. Stürznickel, U. Bechler, K.E. Stockhausen, J. Eissele, J. Hubert, M. Amling, F.T. Beil, B. Busse, T. Rolvien, Impaired bone quality in the superolateral femoral neck occurs independent of hip geometry and bone mineral density, Acta Biomater. 141 (2022) 233–243, https://doi.org/10.1016/j.actbio.2022.01.002.

[10] D.B. Burr, M.R. Allen, Foreword: Calcified Tissue International and Musculoskeletal Research Special Issue: Bone Material Properties and Skeletal Fragility, Calcif. Tissue Int. 97 (2015) 199–200. https://doi.org/10.1007/s00223-015-0012-7.

[11] P. Szulc, A.B. Dufour, M.T. Hannan, D.P. Kiel, R. Chapurlat, E. Sornay-Rendu, B. Merle, S.K. Boyd, D.E. Whittier, D.A. Hanley, D. Goltzman, A.K.O. Wong, E. Lespessailles, S. Khosla, S. Ferrari, E. Biver, M.L. Bouxsein, E.J. Samelson, Fracture risk based on high-resolution peripheral quantitative computed tomography measures does not vary with age in older adults—the bone microarchitecture international consortium prospective cohort study, J. Bone Miner. Res. 39 (2024) 561–570, https://doi.org/10.1093/jbmr/zjae033.

[12] B. Hesse, M. Langer, P. Varga, A. Pacureanu, P. Dong, S. Schrof, N. Man̈nicke, H. Suhonen, C. Olivier, P. Maurer, G.J. Kazakia, K. Raum, F. Peyrin, Alterations of mass density and 3D osteocyte lacunar properties in bisphosphonate-related osteonecrotic human jaw bone, a synchrotron μCT study, PLoS One 9 (2014). https://doi.org/10.1371/journal.pone.0088481.

[13] I. Moreno-Jiménez, S. Heinig, U. Heras, D.S. Maichl, S. Strifler, E. Leich, S. Blouin, P. Fratzl, N. Fratzl-Zelman, F. Jundt, A. Cipitria, 3D osteocyte lacunar morphometry of human bone biopsies with high resolution microCT: from monoclonal gammopathy to newly diagnosed multiple myeloma, Bone 189 (2024), https://doi.org/10.1016/j.bone.2024.117236.

[14] F. Buccino, I. Aiazzi, A. Casto, B. Liu, M.C. Sbarra, G. Ziarelli, G. Banfi, L. M. Vergani, The synergy of synchrotron imaging and convolutional neural networks towards the detection of human micro-scale bone architecture and damage, J. Mech. Behav. Biomed. Mater. 137 (2023), https://doi.org/10.1016/j.jmbbm.2022.105576.

[15] Y. Carter, C.D.L. Thomas, J.G. Clement, A.G. Peele, K. Hannah, D.M.L. Cooper, Variation in osteocyte lacunar morphology and density in the human femur - a synchrotron radiation micro-CT study, Bone 52 (2013) 126–132, https://doi.org/10.1016/j.bone.2012.09.010.

[16] K.S. Mader, P. Schneider, R. Müller, M. Stampanoni, A quantitative framework for the 3D characterization of the osteocyte lacunar system, Bone 57 (2013) 142–154, https://doi.org/10.1016/j.bone.2013.06.026.

[17] E. Goff, F. Buccino, C. Bregoli, J.P. McKinley, B. Aeppli, R.R. Recker, E. Shane, A. Cohen, G. Kuhn, R. Müller, Large-scale quantification of human osteocyte lacunar morphological biomarkers as assessed by ultra-high-resolution desktop micro-computed tomography, Bone 152 (2021), https://doi.org/10.1016/j.bone.2021.116094.

[18] M.P. Akhter, D.B. Kimmel, J.M. Lappe, R.R. Recker, Effect of Macroanatomic Bone Type and Estrogen loss on Osteocyte Lacunar Properties in healthy Adult Women, Calcif. Tissue Int. 100 (2017) 619–630, https://doi.org/10.1007/s00223-017-0247-6.

[19] G. Schröder, K. Denkert, L. Hiepe, M. Schulze, H. Martin, J.R. Andresen, R. Andresen, A. Büttner, H.C. Schober, Histomorphometric analysis of osteocyte density and trabecular structure of 92 vertebral bodies of different ages and genders, Ann. Anat. 246 (2023), https://doi.org/10.1016/j.aanat.2022.152022.

[20] B.R. McCreadie, S.J. Hollister, M.B. Schaffler, S.A. Goldstein, Osteocyte lacuna size and shape in women with and without osteoporotic fracture, in, J. Biomech. (2004) 563–572, https://doi.org/10.1016/S0021-9290(03)00287-2.

[21] E. Goff, A. Cohen, E. Shane, R.R. Recker, G. Kuhn, R. Müller, Large-scale osteocyte lacunar morphological analysis of transiliac bone in normal and osteoporotic premenopausal women, Bone 160 (2022) 116424, https://doi.org/10.1016/j.bone.2022.116424.

[22] O.D. Awosanya, C.E. Dalloul, R.J. Blosser, U.C. Dadwal, M. Carozza, K. Boschen, M. J. Klemsz, N.A. Johnston, A. Bruzzaniti, C.M. Robinson, E.F. Srour, M.A. Kacena, Osteoclast-mediated bone loss observed in a COVID-19 mouse model, Bone 154 (2022), https://doi.org/10.1016/j.bone.2021.116227.

[23] C.-L. Hu, M.-J. Zheng, X.-X. He, D.-C. Liu, Z.-Q. Jin, W.-H. Xu, P.-Y. Lin, J.-W. Cheng, Q.-G. Wei, COVID-19 and bone health, Eur. Rev. Med. Pharmacol. Sci. 27 (2023) 3191–3200, https://doi.org/10.26355/eurrev_202304_31953.

[24] A. Creecy, O.D. Awosanya, A. Harris, X. Qiao, M. Ozanne, A.J. Toepp, M.A. Kacena, T. McCune, COVID-19 and Bone loss: a Review of Risk Factors, Mechanisms, and Future Directions, Curr. Osteoporos. Rep. 22 (2024) 122–134, https://doi.org/10.1007/s11914-023-00842-2.

[25] S. Patel, C. Foster, K. Patel, M. Hunter, C.M. Isales, S. Fulzele, Musculoskeletal Complications in COVID-19: Exploring the Role of Key Biomarkers, Int. J. Mol. Sci. 26 (2025), https://doi.org/10.3390/ijms26178569.

[26] M. Varenna, F. Orsini, R. Di Taranto, F. Zucchi, M. Manara, R. Caporali, C. Crotti, How the COVID-19 pandemic affected bone health: a retrospective, longitudinal study on denosumab persistence from the epicentre of European spreading, Arch. Osteoporos. 18 (2023), https://doi.org/10.1007/s11657-023-01307-w.

[27] F. Buccino, L. Zagra, P. Savadori, A. Galluzzo, C. Colombo, G. Grossi, G. Banfi, L. M. Vergani, Mapping local mechanical properties of human healthy and osteoporotic femoral heads, Materialia (oxf). 20 (2021), https://doi.org/10.1016/j.mtla.2021.101229.

[28] T. Buzug, D. Mihailidis, Computed Tomography from Photon Statistics to Modern Cone-Beam CT, Med. Phys. 36 (2009) 3858, https://doi.org/10.1118/1.3176026.

[29] S. Ma, O. Boughton, A. Karunaratne, A. Jin, J. Cobb, U. Hansen, R. Abel, Synchrotron Imaging Assessment of Bone Quality, Clin. Rev. Bone Miner. Metab. 14 (2016), https://doi.org/10.1007/s12018-016-9223-3.

[30] H.D. Barth, E.A. Zimmermann, E. Schaible, S.Y. Tang, T. Alliston, R.O. Ritchie, Characterization of the effects of x-ray irradiation on the hierarchical structure and mechanical properties of human cortical bone, Biomaterials 32 (2011) 8892–8904, https://doi.org/10.1016/j.biomaterials.2011.08.013.

[31] H.D. Barth, M.E. Launey, A.A. MacDowell, J.W. Ager, R.O. Ritchie, On the effect of X-ray irradiation on the deformation and fracture behavior of human cortical bone, Bone 46 (2010) 1475–1485, https://doi.org/10.1016/j.bone.2010.02.025.

[32] F. Buccino, L. Zagra, E. Longo, L. D'Amico, G. Banfi, F. Berto, G. Tromba, L. M. Vergani, Osteoporosis and Covid-19: Detected similarities in bone lacunar-level alterations via combined AI and advanced synchrotron testing, Mater. Des. 231 (2023), https://doi.org/10.1016/j.matdes.2023.112087.

[33] D. Paganin, S. Mayo, T. Gureyev, P. Miller, S. Wilkins, Simultaneous phase and amplitude extraction from a single defocused image of a homogenous object, J. Microsc. 206 (2002) 33–40, https://doi.org/10.1046/j.1365-2818.2002.01010.x.

[34] F. Brun, S. Pacilè, A. Accardo, G. Kourousias, D. Dreossi, L. Mancini, G. Tromba, R. Pugliese, Enhanced and Flexible Software Tools for X-ray Computed Tomography at the Italian Synchrotron Radiation Facility Elettra, Fundam, Inform 141 (2015) 233–243, https://doi.org/10.3233/FI-2015-1273.

[35] I. Poles, M.D. Santambrogio, E. D'Arnese, Letting Osteocytes Teach SR-MicroCT Bone Lacunae Segmentation: a Feature Variation Distillation Method via Diffusion Denoising, in: M.G. Linguraru, Q. Dou, A. Feragen, S. Giannarou, B. Glocker,

K. Lekadir, J.A. Schnabel (Eds.), Medical Image Computing and Computer Assisted Intervention – MICCAI 2024, Springer Nature Switzerland, Cham, 2024, pp. 383–393.

[36] I. Poles, E. D'Arnese, M. Coggi, F. Buccino, L. Vergani, M.D. Santambrogio, in: A Multimodal Transfer Learning Approach for Histopathology and SR-microCT Low-Data Regimes Image Segmentation, in, Institute of Electrical and Electronics Engineers Inc., 2024, https://doi.org/10.1109/EMBC53108.2024.10781540.

[37] C.M. Heveran, A. Rauff, K.B. King, R.D. Carpenter, V.L. Ferguson, A new open-source tool for measuring 3D osteocyte lacunar geometries from confocal laser scanning microscopy reveals age-related changes to lacunar size and shape in cortical mouse bone, Bone 110 (2018) 115–127, https://doi.org/10.1016/j.bone.2018.01.018.

[38] F. Buccino, S. Bagherifard, L. D'Amico, L. Zagra, G. Banfi, G. Tromba, L.M. Vergani, Assessing the intimate mechanobiological link between human bone micro-scale trabecular architecture and micro-damages, Eng. Fract. Mech. 270 (2022), https://doi.org/10.1016/j.engfracmech.2022.108582.

[39] I. Cruz-Matías, D. Ayala, D. Hiller, S. Gutsch, M. Zacharias, S. Estradé, F. Peiró, Sphericity and roundness computation for particles using the extreme vertices model, J. Comput. Sci. 30 (2019) 28–40, https://doi.org/10.1016/j.jocs.2018.11.005.

[40] M. Fan, D. Su, D. Wu, X. Chen, Reconstruction of irregular elongated/flattened particles and generation of particle aggregates with customizable form distributions, Powder Technol. 425 (2023), https://doi.org/10.1016/j.powtec.2023.118553.

[41] J. Merlo, B. Chaix, M. Yang, J. Lynch, L. Råstam, A brief conceptual tutorial of multilevel analysis in social epidemiology: linking the statistical concept of clustering to the idea of contextual phenomenon, J. Epidemiol. Community Health 59 (2005) (1978) 443–449, https://doi.org/10.1136/jech.2004.023473.

[42] J. Merlo, B. Chaix, H. Ohlsson, A. Beckman, K. Johnell, P. Hjerpe, L. Råstam, K. Larsen, A brief conceptual tutorial of multilevel analysis in social epidemiology: using measures of clustering in multilevel logistic regression to investigate contextual phenomena, J. Epidemiol. Community Health 60 (2006) (1978) 290–297, https://doi.org/10.1136/jech.2004.029454.

[43] C. Peretz, A. Goren, T. Smid, H. Kromhout, Application of Mixed-effects Models for Exposure Assessment, Ann. Occup. Hyg. 46 (2002) 69–77, https://doi.org/10.1093/annhyg/mef009.

[44] M.J. Monsalves, A.S. Bangdiwala, A. Thabane, S.I. Bangdiwala, LEVEL (Logical Explanations & Visualizations of estimates in Linear mixed models): Recommendations for reporting multilevel data and analyses, BMC Med. Res. Methodol. 20 (2020), https://doi.org/10.1186/s12874-019-0876-8.

[45] L. Meteyard, R.A.I. Davies, Best practice guidance for linear mixed-effects models in psychological science, J. Mem. Lang. 112 (2020), https://doi.org/10.1016/j.jml.2020.104092.

[46] G.-W. Sun, T.L. Shook, G.L. Kay, Inappropriate use of bivariable analysis to screen risk factors for use in multivariable analysis, J. Clin. Epidemiol. 49 (1996) 907–916, https://doi.org/10.1016/0895-4356(96)00025-X.

[47] T. Ganesh, L.E. Laughrey, M. Niroobakhsh, N. Lara-Castillo, Multiscale finite element modeling of mechanical strains and fluid flow in osteocyte lacunocanalicular system, Bone 137 (2020) 115328, https://doi.org/10.1016/j.bone.2020.115328.

[48] W. Sang, A. Ural, Quantifying how altered lacunar morphology and perilacunar tissue properties influence local mechanical environment of osteocyte lacunae using finite element modeling, J. Mech. Behav. Biomed. Mater. 135 (2022), https://doi.org/10.1016/j.jmbbm.2022.105433.

[49] S. Blouin, B.M. Misof, M. Mähr, N. Fratzl-Zelman, P. Roschger, S. Lueger, P. Messmer, P. Keplinger, F. Rauch, F.H. Glorieux, A. Berzlanovich, G.M. Gruber, P. C. Brugger, E. Shane, R.R. Recker, J. Zwerina, M.A. Hartmann, Osteocyte lacunae in transiliac bone biopsy samples across life span, Acta Biomater. 157 (2023) 275–287, https://doi.org/10.1016/j.actbio.2022.11.051.

[50] M. Meschia, F. Pansini, A.B. Modena, D. Aloysio, M. Gambacciani, F. Parazzini, C. Campagnoli, G. Maiocchi, E. Peruzzi, Determinants of age at menopause in Italy: results from a large cross-sectional study. ICARUS Study Group. Italian Climacteric Research Group Study, Maturitas 34 (2000) 119–125.

[51] V.T. Carpentier, J. Wong, Y. Yeap, C. Gan, P. Sutton-Smith, A. Badiei, N. L. Fazzalari, J.S. Kuliwaba, Increased proportion of hypermineralized osteocyte lacunae in osteoporotic and osteoarthritic human trabecular bone: Implications for bone remodeling, Bone 50 (2012) 688–694, https://doi.org/10.1016/j.bone.2011.11.021.